Free fermions with dephasing and boundary driving: Bethe Ansatz results

Vincenzo Alba[1*]

1 Dipartimento di Fisica dell' Università di Pisa and INFN, Sezione di Pisa, I-56127 Pisa, Italy
* vincenzo.alba@unipi.it

October 15, 2023

Abstract

By employing the Lindblad equation, we derive the evolution of the two-point correlator for a free-fermion chain of length L subject to bulk dephasing and boundary losses. We use the Bethe ansatz to diagonalize the Liouvillian $\mathcal{L}^{(2)}$ governing the dynamics of the correlator. The majority of its energy levels are complex. Precisely, $L(L-1)/2$ complex energies do not depend on dephasing, apart from a trivial shift. The remaining complex levels are perturbatively related to the dephasing-independent ones for large L. The long-time dynamics is governed by a band of real energies, which contains an extensive number of levels. They give rise to diffusive scaling at intermediate times, when boundaries can be neglected. Moreover, they encode the breaking of diffusion at asymptotically long times. Interestingly, for large loss rate two boundary modes appear in the spectrum. The real energies correspond to string solutions of the Bethe equations, and can be treated effectively for large chains. This allows us to derive compact formulas for the dynamics of the fermionic density. We check our results against exact diagonalization, finding perfect agreement.

1 Introduction

Markovian master equations [1], such as the Lindblad equation, provide a versatile tool to understand the interplay between coherent and dissipative dynamics in *open* quantum many-body systems [2]. Although the interaction with an environment typically is a strong adversary for quantum coherence, it can also be exploited to imprint nontrivial quantum correlations [3], to aid quantum computation [4], or to stabilize topological order [5].

Exact solvable models could potentially help to build a general understanding of open quantum systems, similar to what happened in out-of-equilibrium *closed* systems [6]. Unfortunately, despite intense effort there are comparatively few examples of exact solvable Lindblad equations. Free-fermion and free-boson models subject to arbitrary *linear* jump operators lead to quadratic Liouvillians, and stand out as prominent examples [7]. Still, non quadratic Liouvillians that are solvable, for instance by the Bethe ansatz, exist [8–24]. Remarkably, it has been shown in Ref. [11] that the Liouvillian describing the out-of-equilibrium dynamics of the fermionic tight-binding chain with global dephasing can be mapped to the Hubbard chain with imaginary interaction strength, which can be solved by Bethe ansatz [25]. Interestingly, it is well-established that the dynamics of simple observables, such as few-point correlation functions can be obtained analytically [26–28], without explicitly relying on the exact solvability of the full Liouvillian. Furthermore,
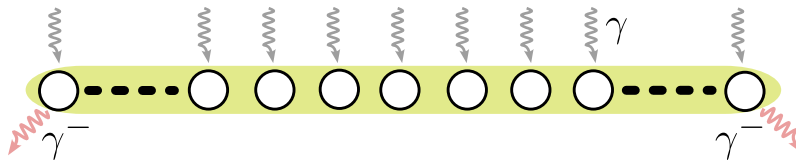
Figure 1: Setup considered in this paper. A tight-binding fermionic chain with L sites is subject to global dephasing, with dephasing rate γ. We employ open boundary conditions. At the edges of the chain fermions are incoherently removed at rate γ^-.

integrability is crucial to devise effective descriptions for out-of-equilibrium open systems. For instance, it has been shown recently that, by exploiting integrability, the Lindblad dynamics of paradigmatic observables can be captured within the hydrodynamic framework [29–34]. For quadratic Liouvillians one can employ the quasiparticle picture [35–37] to describe the dynamics of entanglement-related quantities [38–41]. Similar results were derived for free fermions in the presence of localized dissipation [42–44]. In conclusion, widening the set of integrable Lindblad equations is of paramount importance to make progress in out-of-equilibrium open quantum systems.

Here we provide new results in this direction considering the setup depicted in Fig. 1. We focus on a fermionic tight-binding chain of length L with open boundary conditions. Global dephasing is present on each site of the chain. We denote by γ the dephasing rate. Besides, the chain is subject to incoherent fermion losses with the same rate γ^- at the edges. This prototypical setup was investigated in Ref. [8], and more recently in Ref. [45,46] (see also Ref. [47, 48]). The focus was on the interplay between the diffusive transport induced by the global dephasing and the ballistic one due to the boundary driving. The same setup was employed to study the interplay between dissipation and criticality [2,49]. Here we focus on the two-point fermionic correlation function $G_{x_1,x_2} := \mathrm{Tr}(\rho(t)c^\dagger_{x_1}c_{x_2})$, with c_{x_1}, c_{x_2} standard fermion operators, and $\rho(t)$ the full-system density matrix. The out-of-equilibrium dynamics of G_{x_1,x_2} is governed by a Liouvillian super operator $\mathcal{L}^{(2)}$ (see section 2).

We show that the spectrum, i.e., eigenvalues and eigenvectors, of $\mathcal{L}^{(2)}$ can be constructed explicitly using the Bethe ansatz. This happens despite the fact that the full Liouvillian, to the best of our knowledge, is not integrable. Indeed, as we show, the full Liouvillian is mapped to the one-dimensional Hubbard model with imaginary density-density interaction, imaginary boundary magnetic fields, and imaginary boundary pair production. The last term creates a pair of fermions with opposite spins at the boundaries, making the model non integrable. Since $\mathcal{L}^{(2)}$ is not hermitian, its eigenvalues (energies) are in general complex. The spectrum of $\mathcal{L}^{(2)}$, at least for moderate dephasing rate, splits into three different components. We show that there are $L(L-1)/2$ complex energies that are trivially related by a shift by $-\gamma$ to the energies obtained in the absence of dephasing. These correspond to eigenstates that are free-fermionic in nature. For $\gamma^- = 0$ these energies are purely imaginary forming a vertical band in the complex plane. For nonzero γ^- the band is deformed. Nearby in energy, there are $\sim L(L-1)/2$ complex eigenvalues, which become the same as the dephasing-independent ones in the large L limit.

Finally, a band containing $\sim L$ real energies is present. A similar band is present for periodic boundary conditions (see Ref. [26] and Ref. [28]), where it is responsible for diffusive dynamics at long times. For this reason we dub it diffusive band. The energies with the largest real parts, and the gap of $\mathcal{L}^{(2)}$, are in the diffusive band. The diffusive band correspond to so-called string solutions of the Bethe equations, which in the large L limit can be treated within the framework of the string hypothesis [25]. For instance, this allows us to derive the Liouvillian gap analytically as $\Delta\mathcal{L}^{(2)} = -2\pi^2/(\gamma L^2) + \beta/L^3 + \mathcal{O}(L^{-4})$,

where the constant β, which we determine, depends both on γ and γ^-. The number of energies in the diffusive band depends on γ, γ^-. We show that in the large L limit, i.e., in the regime of validity of the string hypothesis, there is a "critical" $\gamma_c = 4$ above which the band contains the largest number of energies. Upon lowering γ the band gets progressively depleted. In the limit $L \to \infty$ the energies ε in the diffusive band are such that $\varepsilon > \sqrt{\gamma^2 - 16} - \gamma$ for $\gamma > \gamma_c$. The number of levels depends on γ^- as well. Precisely, for $\gamma > \gamma_c$ the band contains L levels for $\gamma^- < \gamma_c^- = \exp(-\text{arccosh}(\gamma/4))$. At larger γ^-, two of the energies detach from the diffusive band, and are pushed to lower energies upon increasing γ^-. The energy splitting between them is exponentially suppressed with L. These eigenvalues correspond to edge modes of $\mathcal{L}^{(2)}$, and are reminiscent of the boundary-related eigenstates of the Hubbard chain with boundary magnetic fields [25].

The Bethe ansatz diagonalization of $\mathcal{L}^{(2)}$ allows, in principle, to obtain the full-time dynamics of $G_{x_1,x_2}(t)$. This is not straightforward because it requires to extract all the L^2 solutions of the Bethe equations. Still, in the long-time limit the dynamics of the correlator is determined by the diffusive band, which can be treated by using the string hypothesis. Here we provide compact expressions for the dynamics of the density profile starting from a fermion localized at an arbitrary site of the chain. This is the main ingredient to obtain the dynamics from an arbitrary initial density profile. At long times, but short enough that the boundaries can be neglected, the density profile exhibits the same diffusive scaling as for periodic boundary conditions. At long time the diffusive regime breaks down due to the boundary losses.

The manuscript is organized as follows. In section 2 we introduce the tight-binding chain with dephasing and boundary losses, and the Lindblad equation. In section 3 we present the Bethe ansatz treatment of the Liouvillian $\mathcal{L}^{(2)}$. Specifically, in section 3.1 we introduce the ansatz for the eigenstates of $\mathcal{L}^{(2)}$. In section 3.2 we derive the Bethe equations. In section 3.3 we discuss the energies that correspond to dephasing-independent solutions of the Bethe equations. In section 3.4 we investigate the eigenvalues of $\mathcal{L}^{(2)}$ that are perturbatively connected to the dephasing-independent ones in the large L limit. Finally in section 3.5 we discuss the diffusive band. In section 4 we focus on the dynamics of the two-point fermionic correlation function. In particular, in section 4.1 we discuss how to expand the initial correlator in the basis of the Bethe states. In section 4.2 we derive the normalization of the Bethe states. In section 4.3, by using the string hypothesis, we derive the long-time limit of the fermion density profile. We discuss numerical results in section 5. Precisely, in section 5.1 we focus on the solution of the Bethe equations. We provide the full set of solutions for chains with $L = 2$ and $L = 3$. In section 5.2 we discuss the solution of the Bethe-Gaudin-Takahashi equation for the diffusive band. In section 5.3 we overview the general structure of the eigenvalues of $\mathcal{L}^{(2)}$ presenting exact diagonalization (ED) data. In section 5.4 we compare the ED data against Bethe ansatz results. In section 5.5 we focus on the finite-size scaling of the Liouvillian gap. In section 5.6 we benchmark the Bethe ansatz results for G_{x_1,x_2} with exact diagonalization. Section 5.7 provides numerical results for the dynamics of the density profile. In section 5.8 we focus on the diffusive scaling of the fermion density and its violation due to the boundary losses. We conclude in section 6. In Appendix A we show that the full Liouvillian of the system is mapped to a one-dimensional Hubbard model with imaginary interaction, imaginary boundary fields and imaginary boundary fermion pair production. In Appendix A.1 we compare the Bethe equations for the Hubbard chain with boundary fields and the Bethe equations derived in section 3.2, showing that they are equivalent.

2 Free fermions with dephasing and boundary losses

Here we consider the fermionic tight-binding chain described by the Hamiltonian

$$H = \sum_{x=1}^{L-1} (c_x^\dagger c_{x+1} + c_{x+1}^\dagger c_x), \tag{1}$$

where $c_x^\dagger, c_x$ are standard fermionic creation and annihilation operators. The system lives on a chain with L sites. We employ open boundary conditions. Our setup is depicted in Fig. 1. The chain undergoes a nonunitary dynamics described by the Lindblad master equation [1]. The state of the system is described by a density matrix $\rho(t)$. Within the framework of Markovian master equations [1], the dynamics of ρ is obtained by solving the Lindblad equation as

$$\frac{d\rho(t)}{dt} := \mathcal{L}(\rho) = -i[H, \rho(t)] + \sum_{x=1}^{L} \sum_{\alpha} \left(L_{x,\alpha} \rho(t) L_{x,\alpha}^\dagger - \frac{1}{2}\{L_{x,\alpha}^\dagger L_{x,\alpha}, \rho(t)\} \right), \tag{2}$$

where $\{,\}$ denotes the anticommutator, and $L_{x,\alpha}$ is the so-called Lindblad operator acting at site x. In (2), $\mathcal{L}$ is the Liouvillian. The label α encodes the different types of dissipation. Specifically, we choose $\alpha = 1$ for global dephasing and $\alpha = 2$ for boundary losses. The Lindblad operator for global dephasing reads as

$$L_{x,1} = \sqrt{\gamma} c_x^\dagger c_x, \quad x \in [1, L]. \tag{3}$$

Localized losses at the edges of the chain are described by

$$L_{x,2} = \sqrt{\gamma^-} c_x, \quad x = 1, L, \tag{4}$$

In (3) and (4), γ and γ^- are the dephasing and loss rates, respectively. By using (2), it is straightforward to obtain the evolution of the fermionic two-point correlation function $G_{x_1,x_2}(t)$ defined as [50]

$$G_{x_1,x_2}(t) := \text{Tr}(\rho(t) c_{x_1}^\dagger c_{x_2}). \tag{5}$$

The dynamics of G_{x_1,x_2} from a generic initial condition $G_{x_1,x_2}(0)$ is obtained by solving the system of equations as [38]

$$\frac{dG_{x_1,x_2}}{dt} := \mathcal{L}^{(2)}(G_{x_1,x_2}) = i(G_{x_1-1,x_2} + G_{x_1+1,x_2} - G_{x_1,x_2-1} - G_{x_1,x_2+1})$$
$$- \gamma G_{x_1,x_2}(1 - \delta_{x_1,x_2}) - \gamma^- G_{x_1,x_2}(\delta_{x_1,1} + \delta_{x_2,1} + \delta_{x_1,L} + \delta_{x_2,L}), \tag{6}$$

where we define the $L^2 \times L^2$ linear super operator $\mathcal{L}^{(2)}$. The superscript in $\mathcal{L}^{(2)}$ is to stress that $\mathcal{L}^{(2)}$ is not the same Liouvillian appearing in (2), which is a $2^L \times 2^L$ matrix and governs the dynamics of the full-system density matrix. In the following we will refer to $\mathcal{L}^{(2)}$ as the Liouvillian, and to $\mathcal{L}$ (cf. (2)) as the full Liouvillian. In (6) we consider the symmetric situation in which the fermions are removed at the edges of the chain at the same rate γ^-. However, the case with different rates $\gamma^-_{L(R)}$ at the left and right edges of the chain can be considered as well. The first term in (6) describes the unitary dynamics governed by the Hamiltonian (1). The second term is the dephasing, which suppresses the off-diagonal elements of G_{x_1,x_2}. The last term describes incoherent absorption of fermions at the edges of the chain.

Importantly, the solution of (6) allows one to obtain the dynamics of G_{x_1,x_2} in several physical situations. For instance, let us consider the setup investigated in Ref. [45], in

which a free-fermion chain is subject to global dephasing and fermion pumping at the left edge of the chain and fermion losses at the right one. Let us focus on the case with dephasing rate γ, and equal pump/loss rate γ'. The evolution of G_{x_1,x_2} is obtained by solving [46]

$$
\frac{dG_{x_1,x_2}}{dt} := \mathcal{L}^{(2)}(G_{x_1,x_2}) = i(G_{x_1-1,x_2} + G_{x_1+1,x_2} - G_{x_1,x_2-1} - G_{x_1,x_2+1})
$$

$$
- \gamma G_{x_1,x_2}(1 - \delta_{x_1,x_2}) - \frac{\gamma'}{2} G_{x_1,x_2}(\delta_{x_1,1} + \delta_{x_2,1} + \delta_{x_1,L} + \delta_{x_2,L}) + \gamma'\delta_{x_1,1}\delta_{x_2,1}. \quad (7)
$$

Eq. (7) is the same as (6) apart for the boundary terms. The boundary dissipation is modeled by the Lindblad operators $L_{x,2} = \sqrt{\gamma'}c_1^\dagger$ and $L_{x,2} = \sqrt{\gamma'}c_L$. Importantly, Eq. (7) becomes the same as (6) after the redefinition $\gamma^- = \gamma'/2$, apart for the "driving" term $\gamma'\delta_{x_1,1}\delta_{x_2,1}$. However, since Eq. (6) and (7) are linear in G_{x_1,x_2}, given the general solution of (6), it is possible to construct the solution of (7) with generic initial condition $G_{x_1,x_2}^{(\mathrm{in})}$. Indeed, let us consider $G_{x_1,x_2}^{(\mathrm{I})}$ solution of (7) without the last term, and with initial condition $G_{x_1,x_2}(0) = G_{x_1,x_2}^{(\mathrm{in})}$. Let us also consider the solution $G_{x_1,x_2}^{(\mathrm{II})}$ of (7) without the driving term and with delta initial condition $G_{x_1,x_2}^{(\mathrm{II})}(0) = \delta_{x_1,1}\delta_{x_2,1}$. Now, one can verify that the solution of (7) is

$$
G_{x_1,x_2}(t) = G_{x_1,x_2}^{(\mathrm{I})} + \gamma' \int_0^t d\tau G_{x_1,x_2}^{(\mathrm{II})}(t - \tau). \quad (8)
$$

In the following sections we will determine the full spectrum, i.e., the eigenvalues and the eigenvectors of $\mathcal{L}^{(2)}$ (cf. (6)), for arbitrary γ, γ^- by using the Bethe ansatz. This allows us to derive compact formulas for the fermionic correlator G_{x_1,x_2} at arbitrary long times and chain sizes. In principle, by using (8) this also allows to obtain the dynamics of G_{x_1,x_2} for the setup of Ref. [45].

3 Bethe Ansatz treatment of the Liouvillian $\mathcal{L}^{(2)}$

Here we discuss the Bethe ansatz framework that allows to solve (6). We first introduce the ansatz *à la* Bethe for the right eigenvectors of $\mathcal{L}^{(2)}$ in section 3.1. In section 3.2 we discuss the solutions of the Bethe equations and the general structure of the eigenvalues (energies) of the Liouvillian $\mathcal{L}^{(2)}$. In section 3.3 we focus on a special class of states, which do not depend on dephasing, i.e., they are the same as in the tight-binding chain with boundary losses. In section 3.4 we discuss eigenvalues of $\mathcal{L}^{(2)}$ that are perturbatively related to the ones of section 3.3 in the large L limit. Finally, in section 3.5 we discuss solutions of the Bethe equations that form perfect strings in the complex plane (see Fig. 2). These states correspond to real energies and govern the long-time dynamics of the fermion correlator.

3.1 Bethe ansatz for the eigenstates of $\mathcal{L}^{(2)}$

Inspired by the coordinate Bethe Ansatz solution of the XXZ chain with open boundary conditions [51] and by the Bethe Ansatz treatment of dephasing [11, 26, 27] and incoherent hopping [28] in free-fermion systems, we employ the following ansatz for G_{x_1,x_2} as

$$
G_{x_1,x_2} = \sum_{r_1,r_2=\pm} r_1 r_2 e^{\varepsilon(k_1,k_2)t} \Big\{ \Big[A_{12}(r_1, r_2)e^{ir_1k_1x_1 + ir_2k_2x_2}
$$

$$
+ (-1)^{x_1+x_2} A_{21}(r_1, r_2)e^{ir_2k_1x_2 + ir_1k_2x_1} \Big]\Theta(x_2 - x_1) + \sigma\Big[A_{12}(r_1, r_2)e^{ir_1k_1x_2 + ir_2k_2x_1}
$$

$$
+ (-1)^{x_1+x_2} A_{21}(r_1, r_2)e^{ir_2k_1x_1 + ir_1k_2x_2} \Big]\Theta(x_1 - x_2) \Big\}. \quad (9)
$$
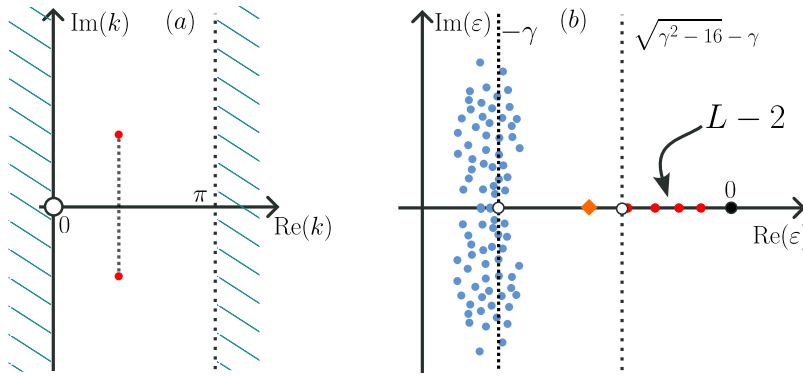
Figure 2: Free-fermion chain with global dephasing and boundary losses. (a) Allowed values for the solutions k_1 and k_2 of the Bethe equations (cf. (18) and (19)). Only the region $0 < \mathrm{Re}(k) < \pi$ is allowed. Some of the solutions form complex conjugate pairs as $k_1 = k_2^*$, corresponding to real energies ε. The remaining solutions are all complex but do not form perfect strings. (b) Typical structure of the Liouvillian spectrum: $\mathrm{Im}(\varepsilon)$ versus $\mathrm{Re}(\varepsilon)$. We only consider the situation with $\gamma > 4$. The red circles are purely real energies. They form an isolated diffusive band of energies. The diffusive band extends up to $\varepsilon = \sqrt{\gamma^2 - 16} - \gamma$, and it contains L energies for generic $\gamma > 4$ and γ^-. Upon lowering γ the diffusive band is depleted. The cluster around $\varepsilon = -\gamma$ contains $\sim L(L-1)$ energies. $L(L-1)/2$ of the levels are trivially obtained from the spectrum of the model at $\gamma = 0$. The diamond denotes a pair of almost degenerate energies, which correspond to boundary-localized modes of the Liouvillian.

Here k_1, k_2 are complex quasimomenta, which have to be determined by solving the so-called Bethe equations. G_{x_1,x_2} (after vectorization) are the right eigenvectors of $\mathcal{L}^{(2)}$ with eigenvalues $\varepsilon(k_1, k_2)$. The evolution of (9) is "simple" because $\mathcal{L}^{(2)}(G_{x_1,x_2}) = \varepsilon G_{x_1,x_2}$, although it is not trivial, due to the energies ε being complex. The sum over r_1, r_2 in (9) is over the reflections of k_1, k_2, similar to the Bethe Ansatz solution of the Heisenberg chain [51] with boundary fields. The functions $\Theta(x)$ are Heaviside step functions. For $x_1 = x_2$, G_{x_1,x_2} is given by the first row in (9). The coefficients A_{12} and A_{21} are scattering amplitudes, which depend on k_1, k_2. Crucially, the Liouvillian $\mathcal{L}^{(2)}$ is invariant under the transformation $\mathcal{R}$ that transforms $G_{x_1,x_2} \to (-1)^{x_1+x_2} G_{x_2,x_1}$ as it can be verified by substitution in (6). Since $\mathcal{R}^2$ is the identity, one has for the eigenfunctions of $\mathcal{R}$ that $(-1)^{x_1+x_2} G_{x_2,x_1} = \sigma G_{x_1,x_2}$, where $\sigma = \pm 1$. The second term in (9) takes into account this symmetry.

To proceed, let us observe that in the bulk of the chain, i.e., for $1 < x_1, x_2 < L$, after substituting (9) in (6), we obtain the condition

$$i(G_{x_1-1,x_2} + G_{x_1+1,x_2} - G_{x_1,x_2-1} - G_{x_1,x_2+1}) - \gamma(1 - \delta_{x_1,x_2})G_{x_1,x_2} - \varepsilon G_{x_1,x_2} = 0. \quad (10)$$

Let us consider the situation with $x_1 \neq x_2$. One can verify that the ansatz (9) satisfies (10) if we fix

$$\varepsilon(k_1, k_2) = 2i\cos(k_1) - 2i\cos(k_2) - \gamma. \quad (11)$$

Importantly, the minus sign in the second term in (11) depends on the choice of the ansatz (9). By redefining $k_2 \to k_2 + \pi$ in the terms that contain the sign factor $(-1)^{x_1+x_2}$ in (9), one obtains that $\varepsilon = 2i\cos(k_1) + 2i\cos(k_2) - \gamma$, which is symmetric under exchange $k_1 \leftrightarrow k_2$ (see, for instance, Ref. [11]). Notice that one has to change $k_2 \to k_2 + \pi$ also in the Bethe equations (see section 3.2). After these redefinitions, the new Bethe equations become the same as the Bethe equations for the Hubbard chain with imaginary boundary

magnetic fields (see Appendix A.1). This happens despite the fact that the full Liouvillian contains a boundary pair production term (see Appendix A).

Let us now determine the coefficients A_{12} and A_{21} in (9). It is convenient to to treat the cases $\sigma = 1$ and $\sigma = -1$ separately. Let us start with the case with $\sigma = 1$ in (9). As it will be clear in section 3.3, for $\sigma = -1$ the ansatz (9) does not depend on γ, and the eigenstates of $\mathcal{L}^{(2)}$ are the same as those of the chain with boundary losses and no bulk dephasing. Let us now impose the "contact" condition obtained by fixing $x_1 = x_2$ in (9). A long calculation gives

$$A_{21}(r_1, r_2) = -A_{12}(r_2, r_1)\frac{\gamma/2 + r_2 \sin(k_1) + r_1 \sin(k_2)}{\gamma/2 - r_2 \sin(k_1) - r_1 \sin(k_2)}. \tag{12}$$

Finally, we impose the boundary conditions. For Eq. (10) to be compatible with the Lindblad equation (6) at the boundaries, we require that

$$iG_{0,x_2} + \gamma^- G_{1,x_2} = 0 \tag{13}$$
$$iG_{x_1,L+1} - \gamma^- G_{x_1,L} = 0. \tag{14}$$

The conditions (13) and (14) give eight equations. They allow us to fix

$$A_{12}(-1, 1) = \frac{1 - ie^{ik_1}\gamma^-}{1 - ie^{-ik_1}\gamma^-} A_{12}(1, 1) \tag{15}$$

$$A_{12}(1, -1) = e^{2ik_2(1+L)}\frac{1 + ie^{-ik_2}\gamma^-}{1 + ie^{ik_2}\gamma^-} A_{12}(1, 1) \tag{16}$$

$$A_{12}(-1, -1) = e^{2ik_2(1+L)}\frac{1 - ie^{ik_1}\gamma^-}{1 - ie^{-ik_1}\gamma^-}\frac{1 + ie^{-ik_2}\gamma^-}{1 + ie^{ik_2}\gamma^-} A_{12}(1, 1). \tag{17}$$

Moreover, one obtains two more equations (Bethe equations) that provide the quantization conditions for k_1 and k_2. Before discussing the Bethe equations, let us stress that it is natural to expect that Eq. (13) and (14) can be modified to account for different loss rates γ_L^- and γ_R^- at the two edges of the chain.

3.2 Bethe equations and general structure of the Liouvillian spectrum

The two extra conditions obtained from (13) and (14) provide two coupled nonlinear equations for k_1, k_2 as

$$e^{2ik_1(L-1)}\Big(\frac{e^{ik_1} - i\gamma^-}{e^{-ik_1} - i\gamma^-}\Big)^2 = \prod_{r_2=\pm 1}\frac{\gamma/2 - \sin(k_1) + r_2\sin(k_2)}{\gamma/2 + \sin(k_1) - r_2\sin(k_2)} \tag{18}$$

$$e^{2ik_2(L-1)}\Big(\frac{e^{ik_2} + i\gamma^-}{e^{-ik_2} + i\gamma^-}\Big)^2 = \prod_{r_1=\pm 1}\frac{\gamma/2 - r_1\sin(k_1) + \sin(k_2)}{\gamma/2 + r_1\sin(k_1) - \sin(k_2)}. \tag{19}$$

Eq. (18) and (19) differ from the Bethe equations for the periodic tight-binding chain with dephasing. For periodic boundary conditions one has that $\gamma^- = 0$ and one has to replace $e^{2ik_j L} \to e^{ik_j L}$. Moreover, only one of the two terms in the right-hand side survives, because there is no product over the reflections of the quasimomenta.

Let us now discuss some properties of the Bethe equations (18) and (19). The total number of solutions is L^2 because the Liouvillian $\mathcal{L}^{(2)}$ is a $L^2 \times L^2$ matrix. The momenta k_1, k_2 are all complex. The allowed domain of k_j is reported in Fig. 2 (a), plotting $\mathrm{Im}(k_j)$ versus $\mathrm{Re}(k_j)$. The Bethe equations possess several symmetries that we now discuss. Given a generic pair of quasimomenta (k_1, k_2) solving (18) and (19), the pairs obtained

by arbitrary reflections $\pm k_1$ and $\pm k_2$ are also solutions of (18) and (19). This can be used to fix $\text{Re}(k_j) > 0$. Notice that $k_j = 0$ and $k_j = \pi$ are solutions of the Bethe equations, although they have to be discarded because they give vanishing eigenvectors (9). The invariance of (18) and (19) under $k_1 \to \pm k_2 \pm \pi$ can be exploited to fix $\text{Re}(k_j) < \pi$. Since the imaginary part of k_j can be arbitrary, the solutions of the Bethe equations live in the strip $(0, \pi) \times (-i\infty, i\infty)$ (see Fig. 2 (a)). Another important property of (18) and (19) is that given a pair (k_1, k_2) solving (18) (19), then (k_2^*, k_1^*), with the star denoting complex conjugation, is also a solution. This means that (cf. (11)) the energies ε appear in complex conjugated pairs.

Crucially, some of the solutions (k_1, k_2) form complex conjugate pairs (see Fig. 2 (a)), i.e., $k_1 = k_2^*$. These solutions form "strings" patterns in the complex plane (see Fig. 2). The corresponding energies are real. We anticipate that these solutions will determine the behavior of the fermionic correlator at long times, because the solutions giving the energies with the larger real parts will be of this type. String solutions of the Bethe equations can be effectively described in the limit $L \to \infty$ by using the framework of the string hypothesis [52]. As we will discuss in section 3.5, in the large L limit the imaginary part of k_1, k_2 can be derived by solving a nonlinear equation, similar to the so-called Bethe-Gaudin-Takahashi (BGT) equation that appears within the framework of the string hypothesis for integrable models [52]. Corrections to the string hypothesis are exponentially suppressed in the limit $L \to \infty$.

Let us now discuss the general structure of the spectrum of $\mathcal{L}^{(2)}$. This is illustrated in Fig. 2 (b). First, for $\gamma^- = 0$, there is a zero-energy state $\varepsilon = 0$, which corresponds to the steady-state of the system at $t \to \infty$. Within the Bethe ansatz treatment, the steady state corresponds to diverging momenta k_1, k_2. At nonzero γ^-, the eigenvalue $\varepsilon = 0$ disappears. We can generically distinguish two different regions in the energy spectrum. The energies ε with the larger real parts form a band of *real* energy near $\varepsilon = 0$. As these solutions are responsible for diffusive behavior [26, 28], we dub them diffusive band [26]. These are reminiscent of the diffusive band appearing for the periodic chain with dephasing [26], or incoherent hopping [28]. The number of energies in the band depends on γ. As it will be clear in the following, for $\gamma > 4$, the diffusive band contains L energies at small γ^-, which is the largest possible number of states. Interestingly, for $\gamma^- > \gamma_c^- = \exp(-\text{arccosh}(\gamma/4))$ (see section 3.5) two of the solutions move outside of the diffusive band towards lower energies (see the diamond symbol in Fig. 2). Concomitantly, the two eigenvalues become almost degenerate. Precisely, their splitting in energy decays exponentially with L. These states are boundary-related, and are present also in the one-dimensional Hubbard model with boundary fields [25]. Boundary-related states have been investigated in the two-particle sector for the open XXZ spin chain in Ref. [53].

Furthermore, a cluster of energies is present around $\varepsilon = -\gamma$. As it will be clear in section 3.3, there are $L(L-1)/2$ energies that are related by a γ shift to the eigenvalues of $\mathcal{L}^{(2)}$ with $\gamma = 0$, i.e., with only losses. Specifically, they are given by (9) with $\sigma = -1$. The associated Bethe equations are decoupled and are given by (24) and (25). The remaining complex energies correspond states with $\sigma = 1$ in (9). Still, in the large L limit they differ from the states with $\sigma = -1$ by $\mathcal{O}(1/L)$ terms, i.e., they are "perturbatively" related to the states with $\sigma = -1$.

3.3 Dephasing-independent solutions

Let us now characterize the states (9) with $\sigma = -1$. Now, the main difference with the case $\sigma = 1$ is that the contact condition (12) has to be modified as

$$A_{21}(r_1, r_2) = -A_{12}(r_2, r_1). \tag{20}$$

The boundary conditions to be imposed are the same as (13) and (14). They give

$$A_{12}(-1,1) = \frac{1 - ie^{ik_1}\gamma^-}{1 - ie^{-ik_1}\gamma^-} A_{12}(1,1) \tag{21}$$

$$A_{12}(1,-1) = \frac{1 + ie^{ik_2}\gamma^-}{1 + ie^{-ik_2}\gamma^-} A_{12}(1,1) \tag{22}$$

$$A_{12}(-1,-1) = \frac{1 - ie^{ik_1}\gamma^-}{1 - ie^{-ik_1}\gamma^-} \frac{1 + ie^{ik_2}\gamma^-}{1 + ie^{-ik_2}\gamma^-} A_{12}(1,1). \tag{23}$$

Notice that there is no dependence on L in (21)-(23), in contrast with the case with $\sigma = 1$. The Bethe equations now read as

$$(\gamma^-)^2 \sin(k_2(1-L)) + 2i\gamma^- \sin(k_2 L) + \sin(k_2(L+1)) = 0 \tag{24}$$

$$(\gamma^-)^2 \sin(k_1(1-L)) - 2i\gamma^- \sin(k_1 L) + \sin(k_1(L+1)) = 0. \tag{25}$$

The Bethe equations for k_1 and k_2 are decoupled, reflecting that the system is noninteracting. Also, k_1, k_2 do not depend on the dephasing rate γ. The energies ε are the same as in (11), implying that the dependence on γ is only a shift. As it is clear from (25), given a solution k_1, then $-k_1$ and $k_1 \pm \pi$ is also a solution. The same holds for k_2. This means that one can restrict to $0 < \mathrm{Re}(k_j) < \pi$. Moreover, the solutions of Eq. (24) and Eq. (25) are related by complex conjugation.

Eq. (24) and (25) are the same equations describing the tight-binding chain with boundary losses and no bulk dephasing [54]. Since Eq. (24) has L solutions $k_1^{(p)}$ with $p = 1, \ldots, L$, the pairs $(k_1^{(p)}, (k_1^{(q)})^*)$ give all the L^2 energies of the Liouvillian. Upon switching on γ, only $L(L-1)/2$ survive. These correspond to the pairs (k_1, k_2) such that $k_j \neq 0, \pi$. Moreover, one has to exclude all the pairs k_1, k_2 such that $k_1 + k_2 = 0 \mod \pi$, and the pairs (k_1', k_2') that are obtained as $(k_1', k_2') = (\pi - k_2, \pi - k_1)$ from a set of solutions (k_1, k_2). Indeed, one can check that the total number of pairs satisfying these constraints is $L(L-1)/2$. Let us also observe that in the limit $L \to \infty$ the solutions of (24) and (25) are given as

$$k_{1,2} = \frac{\pi}{L+1} j_{1,2} + \mathcal{O}(1/L), \quad j_{1,2} = 1, 2, \ldots L. \tag{26}$$

Specifically, the imaginary part of $k_{1,2}$ is $\mathcal{O}(1/L)$, although it is nonzero. Clearly, Eq. (26) is exact without the $\mathcal{O}(1/L)$ correction for $\gamma^- = 0$. In the last case the energies ε are purely imaginary forming a straight line parallel to the imaginary axis (see Fig. 1).

3.4 Solutions with vanishing imaginary parts

Near the energies that correspond to dephasing-independent solutions of the Bethe equations, there are $\sim L(L-1)/2$ energies that correspond to $\sigma = 1$ in (9), and that in the large L limit differ by terms $\mathcal{O}(1/L)$ from the dephasing-independent energies. The number of energies depends on γ. In particular, for $\gamma > 4$ their number is exactly $L(L-1)/2$.

We now discuss them restricting to the case with $\gamma^- = 0$. A similar analysis can be performed for nonzero γ^-. The large L behavior of the Bethe equations (18) (19) suggests the expansion

$$k_1 = k_1^{(r,0)} + k_1^{(r,2)} L^{-2} + i k_1^{(i,1)} L^{-1} \tag{27}$$

$$k_2 = k_2^{(r,0)} + k_2^{(r,2)} L^{-2} + i k_2^{(i,1)} L^{-1}. \tag{28}$$

Here $k_j^{(r,0)}, k_j^{(r,2)}$ and $k_j^{(i,1)}$ ($j = 1, 2$) are real parameters that have to be determined. After substituting the ansatz (27) and (28) in the Bethe equations (18) and (19), Taylor
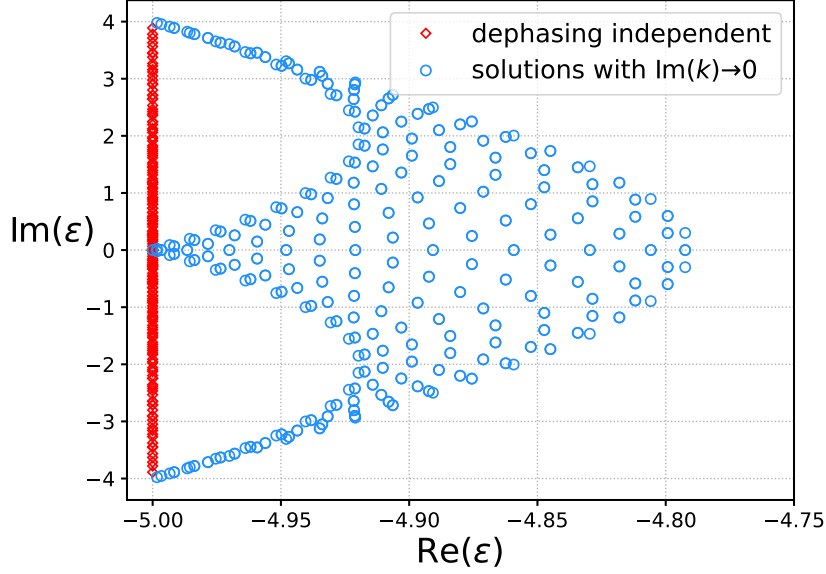
Figure 3: Spectrum of $\mathcal{L}^{(2)}$ for $L = 20$, $\gamma = 5$ and $\gamma^- = 0$. We plot $\text{Im}(\varepsilon)$ versus $\text{Re}(\varepsilon)$. We only show the energies near $\varepsilon = -\gamma$. The circles correspond to the complex solutions (k_1, k_2) of the Bethe equations with vanishing imaginary parts $\text{Im}(k_j) \to 0$ in the limit $L \to \infty$ (see section 3.4). The diamonds are the solutions that do not depend on the dephasing rate γ (see section 3.3).

expanding in the large L limit, and equating the coefficients of the terms with the same powers of L, we obtain

$$2k_1^{(r,0)}(L+1) = j_1\pi, \quad 2k_2^{(r,0)}(L+1) = j_2\pi, \quad \text{with } j_1, j_2 = 1, 2, \ldots 2(L+1). \quad (29)$$

We now provide the expression for $k_j^{(i,1)}$. A similar expression can be obtained for $k_j^{(r,2)}$, although since it is cumbersome we do not report it. We obtain

$$k_1^{(i,1)} = -\frac{1}{2}\frac{L}{L+1}\ln\left[(-1)^{j_1}\frac{\gamma^2 - 2\cos(2k_1^{(r,0)}) + 2\cos(2k_2^{(r,0)}) - 4\gamma\sin(k_1^{(r,0)})}{\gamma^2 - 2\cos(2k_1^{(r,0)}) + 2\cos(2k_2^{(r,0)}) + 4\gamma\sin(k_1^{(r,0)})}\right] \quad (30)$$

$$k_2^{(i,1)} = -\frac{1}{2}\frac{L}{L+1}\ln\left[(-1)^{j_2}\frac{\gamma^2 + 2\cos(2k_1^{(r,0)}) - 2\cos(2k_2^{(r,0)}) + 4\gamma\sin(k_2^{(r,0)})}{\gamma^2 + 2\cos(2k_1^{(r,0)}) - 2\cos(2k_2^{(r,0)}) - 4\gamma\sin(k_2^{(r,0)})}\right]. \quad (31)$$

Consistency with (27) and (28) requires that $k_j^{(i,1)}$ is real. One can readily check that for $\gamma > 4$ the term inside the square brackets in (30) and (31) is positive provided that j_1 and j_2 are both even. For $\gamma < 4$, Eq. (30) and (31) are correct only for the energies near $\varepsilon = -\gamma$. Oppositely, away from $\varepsilon = -\gamma$ the energies are affected by the presence of the diffusive band, and are not accurately described by (30) and (31). Notice that $k_{1,2}^{(i,1)}$ vanish in the large L limit, even at $j_{1,2}/L$ fixed. The energies ε that correspond to solutions of the Bethe equations with vanishing imaginary parts are discussed in Fig. 3. We consider only the case with $\gamma = 5$ because for $\gamma > 4$ the diffusive band at smaller $\text{Re}(\varepsilon)$ is well separated from bulk of the spectrum and (27) and (28) are accurate. The diamonds in the Figure correspond to the eigenstates with $\sigma = -1$ in (9) discussed in section 3.3. The circles are the energies obtained from to momenta of the type (27) and (28). It is interesting to focus on the inner and outer "envelope" of the energies. They are obtained from (29) (30) and (31) as follows. We checked that the levels ε_{in} of the inner envelope correspond to the

choice $j_1 = 2$ and $j_2 \in [2, 2(L+1)]$ and $j_1 \in [2, 2(L+1)]$ in (29). The levels ε_{out} forming the outer envelope are obtained by choosing $j_1 \in [2, 2(L+1)]$ and $j_2 = 2(L+1) - j_1$.

3.5 Diffusive band & boundary states

As we anticipated, the eigenenergies of $\mathcal{L}^{(2)}$ having the largest real part form a diffusive band, and are real. These states correspond to string solutions of the Bethe equations (see Fig. 2 (a)) with nonvanishing imaginary parts in the limit $L \to \infty$. They form complex conjugate pairs (k_1, k_1^*). It is convenient to define $k_1 = k_r + ik_i$ and $k_2 = k_r - ik_i$. We start discussing the case with $\gamma^- = 0$. In terms of k_r, k_i, the Bethe equations (18) and (19) become

$$e^{2(L+1)(ik_r - k_i)} = \frac{(\gamma - 4\cosh(k_i)\sin(k_r))(\gamma - 4i\cos(k_r)\sinh(k_i))}{(\gamma + 4\cosh(k_i)\sin(k_r))(\gamma + 4i\cos(k_r)\sinh(k_i))} \tag{32}$$

$$e^{2(L+1)(ik_r + k_i)} = \frac{(\gamma + 4\cosh(k_i)\sin(k_r))(\gamma - 4i\cos(k_r)\sinh(k_i))}{(\gamma - 4\cosh(k_i)\sin(k_r))(\gamma + 4i\cos(k_r)\sinh(k_i))}. \tag{33}$$

To proceed, we can assume without loss of generality that $k_i > 0$. In the limit $L \to \infty$ the left-hand side of (33) diverges exponentially. This suggests that the denominator in the right-hand side of (32) vanishes. For consistency we can impose that

$$\gamma - 4\cosh(k_i)\sin(k_r) = 0. \tag{34}$$

Solving (34) for k_r, we obtain

$$k_r = \pi - \arcsin\left(\frac{\gamma}{4\cosh(k_i)}\right). \tag{35}$$

To remove the singular denominator in (32) we take the product of (32) and (33), and after using (35), we obtain that k_i satisfies the equation

$$\left(\frac{4}{\gamma\operatorname{sech}(k_i) - i\sqrt{16 - \gamma^2\operatorname{sech}^2(k_i)}}\right)^{4(L+1)} = \left(\frac{\gamma\operatorname{cosech}(k_i) + i\sqrt{16 - \gamma^2\operatorname{sech}^2(k_i)}}{\gamma\operatorname{cosech}(k_i) - i\sqrt{16 - \gamma^2\operatorname{sech}^2(k_i)}}\right)^2. \tag{36}$$

The derivation of (36) is similar to that of the Bethe-Gaudin-Takahashi (BGT) equations for the Hubbard chain [25, 52]. For this reason, we refer to (36) as the BGT equation. The derivation can be extended to the case with nonzero γ^-. The BGT equation becomes

$$\frac{(4e^{k_i} + \gamma\gamma^-\operatorname{sech}(k_i) + i\gamma^-\mathcal{B}(k_i))^2(4e^{-k_i} - \gamma\gamma^-\operatorname{sech}(k_i) - i\gamma^-\mathcal{B}(k_i))^2}{(4e^{k_i}\gamma^- - \gamma\operatorname{sech}(k_i) - i\mathcal{B}(k_i))^2(4e^{-k_i}\gamma^- + \gamma\operatorname{sech}(k_i) + i\mathcal{B}(k_i))^2}$$
$$\times \frac{(\gamma\operatorname{cosech}(k_i) + i\mathcal{B}(k_i))^2}{(\gamma\operatorname{cosech}(k_i) - i\mathcal{B}(k_i))^2} - \left(\frac{4}{\gamma\operatorname{sech}(k_i) - i\mathcal{B}(k_i)}\right)^{4L} = 0, \tag{37}$$

where we defined

$$\mathcal{B}(x) := \sqrt{16 - \gamma^2\operatorname{sech}^2(x)}. \tag{38}$$

After solving (37) for k_i, we obtain k_r by using (35). It is convenient to take the logarithm of both terms in (37) to obtain the BGT equations in logarithmic form. Let us first define

$$z := \frac{\gamma}{4\cosh(k_i)}, \quad k_i = \operatorname{arccosh}\left(\frac{\gamma}{4z}\right). \tag{39}$$

After taking the logarithm of both members in (37) and using (39), we obtain

$$
2iL\arcsin(z_j) + \ln\left[\frac{z_j\gamma + i\sqrt{1-z_j^2}\sqrt{\gamma^2-16z_j^2}}{z\gamma - i\sqrt{1-z_j^2}\sqrt{\gamma^2-16z_j^2}}\right]
$$

$$
+ \ln\left[\frac{\gamma^-(-iz_j + \sqrt{1-z_j^2})(\gamma + \sqrt{\gamma^2-16z_j^2}) + 4iz_j}{(iz_j - \sqrt{1-z_j^2})(\gamma + \sqrt{\gamma^2-16z_j^2}) + 4iz_j\gamma^-}\right]
$$

$$
+ \ln\left[\frac{\gamma + \sqrt{\gamma^2-16z_j^2} + 4z_j(z_j + i\sqrt{1-z_j^2})\gamma^-}{4z_j(z_j + i\sqrt{1-z_j^2}) - (\gamma + \sqrt{\gamma^2-16z_j^2})\gamma^-}\right] = -\pi i I_j. \quad (40)
$$

Here $I_j \in [0, L-2)$ are integers, forming the so-called BGT quantum numbers, which identify the different solutions z_j. They originate from the branch cut of the logarithm. The energy with the largest real part corresponds to $I_j = 0$. Notice that here we assume $\gamma^- > 0$. For $\gamma^- = 0$ $I_j = 0$ has to be excluded, because it would correspond to $\varepsilon = 0$. The number of solutions in the diffusive band depends on γ and γ^-. Specifically, for $\gamma > 4$ there are at least $L-2$ solutions of (40). Two extra solutions appear provided that γ^- is small enough. Precisely, for $\gamma^- > \gamma_c^-$ two of the energies detach from the diffusive band, moving towards lower energies. They correspond to boundary-related modes of the Liouvillian $\mathcal{L}^{(2)}$ (see diamond symbol in Fig. 2). Similar boundary states appear in the open Hubbard chain with boundary magnetic fields [25]. Precisely, from (37) we obtain that the boundary-related states are present for $\gamma^- > \gamma_c^-$ given as

$$
\gamma_c^- = \exp\left(-\mathrm{arccosh}(\gamma/4)\right). \quad (41)
$$

The condition (41) is obtained by noticing that at the left edge of the diffusive band (see Fig. 2) one has that $k_i = \mathrm{arccosh}(\gamma/4)$, and by solving Eq. (37) for γ^-. Eq. (41) holds true for $\gamma > 4$, and, since we are employing the framework of the string hypothesis, in the thermodynamic limit $L \to \infty$. Finally, we should stress that to extract the quasimomenta that correspond to the boundary-related energies it is convenient to use Eq. (37) rather than the logarithmic BGT equation (40), as it will be clear in section 5.2 (see Fig. 6).

Let us now discuss the gap of the Liouvillian $\mathcal{L}^{(2)}$. This is obtained by considering the energy ε with the smallest nonzero real part. Precisely, the gap $\Delta\mathcal{L}^{(2)}$ is defined as

$$
\Delta\mathcal{L}^{(2)} := -\max_j \mathrm{Re}(\varepsilon_j), \quad \text{with } \mathrm{Re}(\varepsilon_j) \neq 0. \quad (42)
$$

We numerically verified that for nonzero γ^-, $\Delta\mathcal{L}^{(2)}$ corresponds to $I_j = 0$ in (40). For $\gamma^- = 0$ one has to choose $I_j = 1$. Focusing on $\gamma^- \neq 0$, a straightforward expansion of (40) for $I_j = 0$ in the large L limit gives

$$
z \simeq \frac{\pi}{2}\frac{1}{L} + \left(\frac{\pi}{2} - \frac{\pi(1-(\gamma^-)^2)}{\gamma\gamma^-}\right)\frac{1}{L^2}, \quad (43)
$$

where we neglected higher order terms in $1/L$. After substituting in the expression for the energy (11) we obtain the gap of the Liouvillian as

$$
\Delta\mathcal{L}^{(2)} \simeq -\frac{2\pi^2}{\gamma L^2} + \frac{4\pi^2(2 - \gamma\gamma^- + 2(\gamma^-)^2)}{\gamma^2\gamma^-}\frac{1}{L^3}. \quad (44)
$$

At the leading order in $1/L$, the gap depends only on the bulk dephasing. At higher orders a dependence on γ^- appears. This reflects that the effect of the boundaries appear at later times.

4 Asymptotic dynamics of the fermionic two-point function

Here we derive a formula for the time-dependent correlation function $G_{x_1,x_2}(t)$ starting from an arbitrary initial condition $G_{x_1,x_2}(0)$. The strategy is to build a complete basis of operators by using the Bethe states (9). This basis is then used to expand the initial condition for the correlator. In section 4.1 we construct the complete basis for the generic two-point correlation function, using the left and right eigenvectors of $\mathcal{L}^{(2)}$. In section 4.2 we compute the leading contribution of the norm of the Bethe states (9) in the large L limit. We only consider the states forming the diffusive band, because they are dominant in the long-time limit. Finally, in section 4.3 we derive the long-time limit of the density profile, i.e., the diagonal correlator $G_{x,x}(t)$.

4.1 Left and right eigenvectors of $\mathcal{L}^{(2)}$

One can decompose the initial correlator $G_{x_1,x_2}(0)$ in the basis of eigenvectors of $\mathcal{L}^{(2)}$. Let us denote with $G_{x_1,x_2}^{(k_1,k_2)}$ the eigenvector of $\mathcal{L}^{(2)}$ identified by the solutions k_1, k_2 of the Bethe equations (18) (19). The dynamics of $G_{x_1,x_2}^{(k_1,k_2)}$ is given as

$$\frac{dG_{x_1,x_2}^{(k_1,k_2)}}{dt} = \mathcal{L}^{(2)}(G_{x_1,x_2}^{(k_1,k_2)}) = \varepsilon(k_1,k_2)G_{x_1,x_2}^{(k_1,k_2)}. \tag{45}$$

The generic correlator G_{x_1,x_2} can be decomposed as

$$G_{x_1,x_2}(t) = \sum_{\{k_1,k_2\}} |k_1,k_2\rangle\langle k_1,k_2|0\rangle e^{\varepsilon(k_1,k_2)t}, \quad |k_1,k_2\rangle := N_{k_1,k_2}^{-1} G_{x_1,x_2}^{(k_1,k_2)}. \tag{46}$$

where the sum is over the solutions of the Bethe equations $\{k_1,k_2\}$ (cf. (18) and (19)). In (46) we redefined $|0\rangle := G_{x_1,x_2}(0)$, and we defined $\langle k_1,k_2| := \bar{G}_{x_1,x_2}^{(k_1,k_2)}$ as the left eigenvector of the Liouvillian. Since the Liouvillian is not hermitian we have that $\langle k_1,k_2| \neq (|k_1,k_2\rangle)^\dagger$. In (46) we defined the "scalar product"

$$\langle k_1,k_2|k_3,k_4\rangle := \sum_{z_1,z_2=1}^{L} \bar{G}_{z_1,z_2}^{(k_1,k_2)} G_{z_1,z_2}^{(k_3,k_4)}. \tag{47}$$

Similar definition holds for the scalar product with the initial correlator $|0\rangle$, i.e., $\langle k_1,k_2|0\rangle$. In (46) $N_{k_1,k_2} := \langle k_1,k_2|k_1,k_2\rangle$ is the normalization of the eigenvectors. Since $\mathcal{L}^{(2)}$ is a symmetric matrix, a naive choice would be $\bar{G}_{x_1,x_2}^{(k_1,k_2)} = G_{x_1,x_2}^{(k_1,k_2)}$. Again, as the Liouvillian is not hermitian, this choice yields vanishing norm for the eigenstates. Following Ref. [28], it is possible to determine a more convenient choice for $\langle k_1,k_2|$ by observing that the energy (11) is invariant under the redefinition

$$k_1 = \pi - k_2, \quad k_2 = \pi - k_1. \tag{48}$$

This suggests to define

$$\langle k_1,k_2| := |\pi - k_2, \pi - k_1\rangle. \tag{49}$$

Under the redefinition (48), the ansatz (9) gets modified. Apart from the redefinition (48), one obtains new scattering amplitudes $\bar{A}_{12}$ and $\bar{A}_{21}$. For $\sigma = 1$ they read as

$$\bar{A}_{21}(r_1,r_2) = -\bar{A}_{12}(r_2,r_1)\frac{\gamma/2 + r_1\sin(k_1) + r_2\sin(k_2)}{\gamma/2 - r_1\sin(k_1) - r_2\sin(k_2)}. \tag{50}$$

Notice that (50) differs from (12) by the exchange $r_1 \leftrightarrow r_2$ in the ratio on the right-hand side. Moreover, we have that

$$\bar{A}_{12}(-1,1) = \frac{1 + ie^{-ik_2}\gamma^-}{1 + ie^{ik_2}\gamma^-}\bar{A}_{12}(1,1) \tag{51}$$

$$\bar{A}_{12}(1,-1) = e^{-2ik_1(L+1)}\frac{1 - ie^{ik_1}\gamma^-}{1 - ie^{-ik_1}\gamma^-}A_{12}(1,1) \tag{52}$$

$$\bar{A}_{12}(-1,-1) = e^{-2ik_1(L+1)}\frac{1 - ie^{ik_1}\gamma^-}{1 - ie^{-ik_1}\gamma^-}\frac{1 + ie^{-ik_2}\gamma^-}{1 + ie^{ik_2}\gamma^-}\bar{A}_{12}(1,1). \tag{53}$$

Importantly, the Bethe equations remain the same as in (18) and (19).

Let us now discuss the case of $\sigma = -1$. Repeating the steps as above we obtain that

$$\bar{A}_{21}(r_1,r_2) = -\bar{A}_{12}(r_2,r_1). \tag{54}$$

Moreover, we have

$$\bar{A}_{12}(-1,1) = \frac{1 + ie^{-ik_2}\gamma^-}{1 + ie^{ik_2}\gamma^-}\bar{A}_{12}(1,1) \tag{55}$$

$$\bar{A}_{12}(1,-1) = \frac{1 - ie^{-ik_1}\gamma^-}{1 - ie^{ik_1}\gamma^-}\bar{A}_{12}(1,1,) \tag{56}$$

$$\bar{A}_{12}(-1,-1) = \bar{A}_{12}(1,-1)\bar{A}_{12}(-1,1)/\bar{A}_{12}(1,1). \tag{57}$$

We anticipate, however, that since the states with $\sigma = -1$ have typically small $\text{Re}(\varepsilon)$, they do not contribute significantly at long times. Moreover, for delta initial conditions $G_{x_1,x_2}(0)$ considered in section 4.3 their contribution is exactly zero.

4.2   Norm of the eigenvectors

Here we derive the norm N_{k_1,k_2} for a Bethe eigenstate (9) characterized by generic solutions of the Bethe equations k_1, k_2. To proceed, let us focus on eigenstates with $\sigma = 1$ (cf. (9)) because they dominate the dynamics at long times. By using (9) (47) and (49) we obtain that

$$N_{k_1,k_2} = \langle k_1, k_2 | k_1, k_2 \rangle = N_0 + N_1 L + N_2 L^2, \tag{58}$$

where N_0, N_1, N_2 are functions of k_1, k_2. A tedious calculation gives

$$N_2 = -8\frac{\gamma/2 + \sin(k_1) + \sin(k_2)}{\gamma/2 - \sin(k_1) - \sin(k_2)}. \tag{59}$$

A similar calculation gives N_1 as

$$N_1 = 4i\gamma(\cos(k_1) - \cos(k_2))\left[\frac{1}{(\gamma/2 - \sin(k_1) - \sin(k_2))^2}\right.$$
$$+ \frac{\gamma/2 + \sin(k_1) + \sin(k_2)}{(\gamma/2 - \sin(k_1) - \sin(k_2))(\gamma/2 - \sin(k_1) + \sin(k_2))(\gamma/2 + \sin(k_1) - \sin(k_2))}\right]$$
$$- \frac{\gamma/2 + \sin(k_1) + \sin(k_2)}{\gamma/2 - \sin(k_1) - \sin(k_2)}\left[\frac{8(1 + (\gamma^-)^2)}{(1 - i\gamma^-e^{ik_1})(1 - i\gamma^-e^{-ik_1})}\right.$$
$$\left.+ \frac{8(1 + (\gamma^-)^2)}{(1 + i\gamma^-e^{ik_2})(1 + i\gamma^-e^{-ik_2})}\right]. \tag{60}$$

Finally, we observe that N_0 is in general nonzero. This is in contrast with the case of the tight-binding chain with incoherent hopping and periodic boundary conditions [28].

Crucially, we notice that for the string solutions of the Bethe equations forming the diffusive band (see section 3.5) both N_1 and N_2 are singular in the limit $L \to \infty$ because $\gamma/2 - \sin(k_1) - \sin(k_2)$ vanishes. Similar divergences will plague the overlaps $\langle k_1, k_2 | 0 \rangle$ and $|k_1, k_2\rangle$. This means that to extract the dynamics of G_{x_1, x_2} one has to take carefully the limit $L \to \infty$, i.e., going beyond the string hypothesis. In the following section we will show that to obtain the leading behavior of the norm in the large L limit it is sufficient to consider the term in (60).

4.3 Evolution of the density profile

In this section we provide analytic results for the dynamics of $G_{x,x}(t)$ starting from the initial condition

$$|0\rangle := G_{x_1, x_2}(0) = \delta_{x_1, x} \delta_{x_2, x}, \tag{61}$$

which corresponds to a fermion initially localized at position x. Our results hold in the long-time limit and for large L.

Crucially, since Eq. (6) is linear as a function of G_{x_1, x_2}, its solution with the delta initial condition (61) is sufficient to obtain the dynamics of G_{x_1, x_2} starting from an arbitrary initial density profile. Precisely, let us consider a generic diagonal initial condition as

$$|0\rangle = \delta_{x_1, x_2} f(x_2), \tag{62}$$

where $0 \le f(x) \le 1$. Given the solution $G_{x_1, x_2}^{(x)}(t)$ with initial condition (61) at fixed x, the solution $G_{x_1, x_2}(t)$ with initial condition (62) is obtained as

$$G_{x_1, x_2}(t) = \sum_{x=1}^{L} G_{x_1, x_2}^{(x)}(t). \tag{63}$$

Let us now discuss the time-dependent correlator $G_{x_1, x_2}(t)$ starting from (61). To be specfic, let us consider the situation with a fermion initially localized at x away from the boundaries, i.e., with $x/L \ne 0, 1$ in (61). To obtain $G_{x_1, x_2}(t)$ we employ (46), restricting ourselves to the eigenstates of the Liouvillian forming the diffusive band (see section 3.5). Moreover, we exploit the string hypothesis, which holds in the limit $L \to \infty$. A straightforward calculation gives the overlaps between (61) and the generic Bethe eigenstate (9) as

$$\langle k_1, k_2 | 0 \rangle = \sum_{r_1, r_2 = \pm} r_1 r_2 \left[e^{-i(r_2 k_1 + r_1 k_2)x} \bar{A}_{12}(r_1, r_2) + e^{-i(r_1 k_1 + r_2 k_2)x} \bar{A}_{21}(r_1, r_2) \right], \tag{64}$$

where we used (49) and (48). Eq. (64) is valid for all the Bethe eigenstates (9). However, it is straightforward to check that the eigenstates with $\sigma = -1$ (see section (24)) have zero overlap with (61).

Let us now restrict ourselves to the eigenstates forming the diffusive band (see Fig. 2 (b)). As discussed in section 3.5, the corresponding solutions of the Bethe equations form complex conjugated pairs, and can be treated by means of the string hypothesis. As anticipated in section 4.2, an important issue is that upon substituting the solutions of the BGT equation (40) in the expression for $|k_1, k_2\rangle$, $\langle k_1, k_2|$, spurious divergences appear. The divergences are due to the presence of the term $(\gamma/2 - \sin(k_1) - \sin(k_2))^{-1}$. Moreover, both N_1 and N_2 in (59) and (60) diverge as well. To solve this issue, one can first exploit the invariance under reflections of k_1, k_2. Specifically, it is convenient to consider new quasimomenta

$$k_1 \to k_1, \quad k_2 \to -k_2. \tag{65}$$

After using (65), one obtains that the term $(\gamma/2 - \sin(k_1) + \sin(k_2))^{-1}$ is singular. This is convenient because now only N_1 is singular, whereas N_2 (cf. (59)) is regular. To proceed, one has to determine the singularities of $|k_1, k_2\rangle$, $\langle k_1, k_2|$. The singularity structure of the terms entering in $|k_1, k_2\rangle$ (cf. (9)) is given as

$$e^{-ik_1 x_1 - ik_2 x_2} A_{12}(-,-) \simeq \delta^{1-(x_1+x_2)/(2L)} \tag{66}$$

$$e^{-ik_1 x_1 + ik_2 x_2} A_{12}(-,+) \simeq \delta^{-(x_1-x_2)/(2L)} \tag{67}$$

$$e^{ik_1 x_1 - ik_2 x_2} A_{12}(+,-) \simeq \delta^{1+(x_1-x_2)/(2L)} \tag{68}$$

$$e^{ik_1 x_1 + ik_2 x_2} A_{12}(+,+) \simeq \delta^{(x_1+x_2)/(2L)}, \tag{69}$$

where we assume $x_1 \leq x_2$, and we defined δ as

$$\delta = \gamma/2 - \sin(k_1) + \sin(k_2). \tag{70}$$

Notice that $\delta = \mathcal{O}(e^{-aL})$, with $a > 0$. A similar result can be obtained for the terms with scattering amplitudes A_{21} (cf. (9)). Importantly, to derive (66) (67) (68) (69), we employed the Bethe equations (18) and (19) to write the diverging contributions $e^{ik_j L}$ in terms of δ. To proceed, we observe that a similar calculation can be done for the contributions appearing in $\langle k_1, k_2|$. Now, upon taking the limit $\delta \to 0$ the singularities cancel out. Precisely, the term N_1 in the norm (59) diverges as δ^{-1}, implying that (cf. (46)) $|k_1, k_2\rangle\langle k_1, k_2|0\rangle = \mathcal{O}(\delta^{-1})$ for any k_1, k_2 satisfying the BGT equation (40). A straightforward calculation shows that the only possibility is that $\langle k_1, k_2|0\rangle = \mathcal{O}(\delta^{-1})$ and $|k_1, k_2\rangle = \mathcal{O}(1)$. Precisely, only the term with $A_{12}(-,+)$ (cf. (9)) survives in $|k_1, k_2\rangle$. Similarly, one has to keep only the terms with $\bar{A}_{12}(+,-)$ and $\bar{A}_{21}(+,-)$ in the overlap $\langle k_1, k_2|0\rangle$. After removing the singularities, the fermionic density $G_{x1,x1}$ is given as

$$G_{x_1,x_1} = \sum_{\{k_1,k_2\}} \widetilde{N}_1^{-1} e^{i(k_2-k_1)x_1} B_{12}(-,+)\bar{g}_{x,x}. \tag{71}$$

The sum in (71) is over the eigenstates of $\mathcal{L}^{(2)}$ forming the diffusive band (see section 3.5), and which are treated within the framework of the string hypothesis. In (71) we defined

$$B_{12}(-,+) = \frac{e^{ik_1}(1 - ie^{-ik_1}\gamma^-)}{e^{ik_1} - i\gamma^-}. \tag{72}$$

In (71) $\bar{g}_{x,x}$ is the finite part of the overlap with the initial condition, and it reads as

$$\bar{g}_{x,x} = e^{i(k_1-k_2)x}\bar{B}_{12}(+,-) + e^{-i(k_1-k_2)z}\bar{B}_{21}(+,-), \tag{73}$$

where

$$\bar{B}_{12}(+,-) = \frac{1 - i\gamma^- e^{-ik_1}}{1 - i\gamma^- e^{ik_1}} \frac{\gamma/2 + \sin(k_1) - \sin(k_2)}{\gamma/2 - \sin(k_1) - \sin(k_2)}(\gamma + 2\sin(k_1) + 2\sin(k_2)) \tag{74}$$

$$\bar{B}_{21}(+,-) = -\frac{1 + i\gamma^- e^{ik_2}}{1 + i\gamma^- e^{-ik_2}}(\gamma + 2\sin(k_1) - 2\sin(k_2)). \tag{75}$$

Finally, the finite part of the normalization $\widetilde{N}_1^{-1}$ in (71) is given as

$$\widetilde{N}_1^{-1} = \frac{4i\gamma(\cos(k_1) - \cos(k_2))(\gamma + \sin(k_1) + \sin(k_2))}{(\gamma/2 + \sin(k_1) - \sin(k_2))(\gamma/2 - \sin(k_1) - \sin(k_2))}L. \tag{76}$$

Again, Eq. (71) should hold in the long-time limit, provided that L is large enough to ensure the validity of the string hypothesis.

5 Numerical results

Here we provide numerical results supporting the Bethe ansatz treatment of the previous sections. First, in section 5.1 we discuss the numerical solution of the Bethe equations (18) and (19). In section 5.2 we focus on the Bethe-Gaudin-Takahashi equation (37) and (40). In section 5.3 we discuss exact diagonalization data for the eigenvalues of $\mathcal{L}^{(2)}$. In section 5.4 we compare the spectrum of $\mathcal{L}^{(2)}$ obtained from exact diagonalization with the Bethe ansatz results. In section 5.5 we investigate the finite-size scaling of the Liouvillian gap. In section 5.6 we address the dynamics of the *full* correlator G_{x_1,x_2} (cf. (6)). In section 5.7 we focus on the profile of the fermion density. Finally, in section 5.8 we discuss the diffusive scaling of the fermion density and its violation due to the boundary losses.

5.1 Numerical solution of the Bethe equations

The numerical solution of the Bethe equations is in general a challenging task. Indeed, Eq. (18) and (19) have L^2 solutions in the complex plane. Moreover, $k_1 = 0$ and $k_2 = 0$, as well as $k_1 = \pi$ and $k_2 = \pi$ are always solutions, although they have to be excluded because they correspond to vanishing eigenvectors. Similarly, the solutions with $k_1 = k_2$ have to be excluded. Pairs of solutions (k_1, k_2) that are related by a shift by $\pm\pi$ have to be counted only once. Crucially, since all the solutions of (18) and (19) are complex, multiple-precision arithmetic is necessary to evaluate the exponentials in the left-hand side of the equations.

Solutions of Bethe equations for $L = 2$ and $L = 3$, with $\gamma = \gamma^- = 1/10$

L	σ	k_1	k_2	ε
2	+	$2.1919997294 - 0.1312558459i$	$1.1457120114 - 0.0351640458i$	$-0.25 - 1.9993749023i$
2	+	$1.1457120114 + 0.0351640458i$	$2.1919997294 + 0.1312558459i$	$-0.25 + 1.9993749023i$
2	+	$0.7866450552 - 0.0353040029i$	$0.7866450552 + 0.0353040029i$	-0.2
2	−	$2.0934365739 - 0.0576711461i$	$2.0934365739 + 0.0576711461i$	-0.3
3	+	$1.28745845407 - 0.04147721049i$	$1.28745845407 + 0.04147721049i$	-0.2593393435
3	+	$2.67275603750 + 0.00860942154i$	$2.67275603750 - 0.00860942154i$	-0.1155608174
3	+	$2.28508055892 + 0.03633954446i$	$0.71654617450 + 0.08931362935i$	$-0.162549919 - 2.8251952277i$
3	+	$0.71654617450 - 0.08931362935i$	$2.28508055892 - 0.03633954446i$	$-0.162549919 + 2.8251952277i$
3	+	$2.36338604213 - 0.06913029032i$	$1.57756565342 + 0.0014316741i$	$-0.2 - 1.4142135623i$
3	+	$1.5775656534 - 0.00143167416i$	$2.36338604213 + 0.0691302903i$	$-0.2 + 1.4142135623i$
3	−	$0.7866450552 - 0.0353040029i$	$0.78664505521 + 0.03530400298i$	-0.2
3	−	$1.5707963267 - 0.0499791900i$	$2.35494759837 + 0.03530400298i$	$-0.25 + 1.4133294025i$
3	−	$2.3549475983 - 0.0353040029i$	$1.57079632679 + 0.04997919006i$	$-0.25 - 1.4133294025i$

Table 1: Full set of solutions of the Bethe equations (cf. (18)(19)) for with $L = 2$ (first four rows) and $L = 3$ (last nine rows) sites, and with $\gamma = \gamma^- = 1/10$. We show the two quasimomenta k_1, k_2 and the associated energy ε. The last solution for $L = 2$ and the last three solutions for $L = 3$ correspond to $\sigma = -1$ in (9), i.e., they are the same as for $\gamma = 0$. Notice that by using the symmetries of the Bethe equations, we fix $0 < \text{Re}(k_1) < \pi$ and $0 < \text{Re}(k_2) < \pi$. Given a set of solutions (k_1, k_2), one has that (k_2^*, k_1^*) is also a solution. Notice that for $\sigma = -1$ only $L(L - 1)/2$ solutions are allowed.

To illustrate the structure of the solutions of the Bethe equations, it is useful to focus on chains with small L. In Table 1 we show the full set of solutions of (18) and (19) for $L = 2$ and $L = 3$. We only a consider fermionic chain with open boundary conditions and $\gamma = \gamma^- = 1/10$. The second column of the table shows the eigenvalues of σ (cf. (9)). The states with $\sigma = -1$ are not affected by dephasing, as discussed in section 3.3. The number of solutions with $\sigma = -1$ is $L(L - 1)/2$. The third and fourth column show the solutions (k_1, k_2) of the Bethe equations. Importantly, the invariance of (18) and (19)
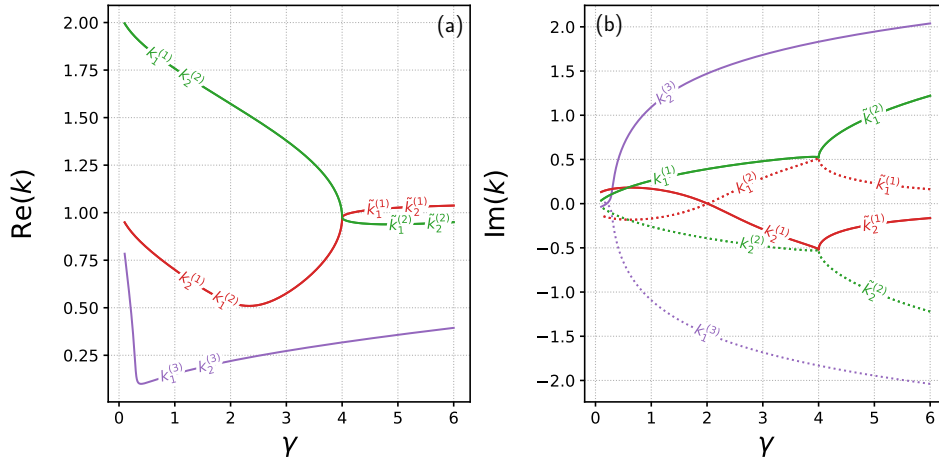
Figure 4: Solutions (k_1, k_2) of the Bethe equations (18) and (19) for $L = 2$ and fixed $\gamma^- = 1/10$. We only consider solutions with $\sigma = 1$ (cf. (9)). We plot (k_1, k_2) as functions of the dephasing rate γ. Panel (a) shows the real parts of k_1 and k_2, the imaginary parts being reported in panel (b). Starting from $\gamma = 0$ one has the three pairs $(k_1^{(j)}, k_2^{(j)})$ with $j = 1, 2, 3$. The solutions with $j = 1, 2$ are related by $(k_1^{(1)}, k_2^{(1)}) = (k_2^{(2)}, k_1^{(2)})^*$, with the star denoting complex conjugation. The solution with $j = 3$ is such that $k_1^{(3)} = (k_2^{(3)})^*$. At $\gamma = 4$ the solutions with $j = 1, 2$ "collide". The solutions at $\gamma > 4$ are denoted with a tilde. At $\gamma > 4$ all the solutions are formed by complex conjugate pairs, i.e., $\tilde{k}_1^{(j)} = (\tilde{k}_2^{(j)})^*$ for any j.

under the change of sign of k_j and under shifts by π can be used to fix $0 < \mathrm{Re}(k_j) < \pi$. Notice also that the Bethe equations are not invariant under exchange $k_1 \leftrightarrow k_2$. However, given a solution (k_1, k_2), then (k_2^*, k_1^*), with the star denoting complex conjugation, is also a solution. As it is clear from (1), some of the solutions are formed by pairs of complex conjugated momenta (k_1, k_1^*). These correspond to the real eigenvalues ε of $\mathcal{L}^{(2)}$. The last column in Table 1 is the energy ε as obtained by using (11). We checked that the energies coincide with the exact diagonalization results to machine precision.

It is interesting to investigate how the solutions of the Bethe equations change as a function of dissipation. In Fig. 4 we show the solutions of the Bethe equations for $L = 2$ at fixed $\gamma^- = 1/10$ as a function of γ. We only consider the three solutions with $\sigma = 1$ (cf. (9) and Table 1). Panel (a) and (b) show $\mathrm{Re}(k_j)$ and $\mathrm{Im}(k_j)$ as a function of γ. We consider the interval $\gamma \in [1/10, 6]$. We denote the different solutions as $(k_1^{(p)}, k_2^{(p)})$, with $p \in [1, 3]$. Now, the solution at the bottom in Fig. 4 (a), i.e., with $p = 3$, corresponds to $k_2 = k_1^*$, i.e., to real energy ε. The remaining two solutions are such that $k_1^{(1)} = (k_2^{(2)})^*$ and $k_1^{(2)} = (k_2^{(1)})^*$. Interestingly, the behavior of the solutions as a function of γ is not "smooth". Precisely, at $\gamma = 4$ the solutions with $p = 1$ and $p = 2$ "collide", whereas the one with $p = 3$ remains isolated. At $\gamma > 4$ the solutions with $p = 1, 2$ get reorganized. Precisely, they emerge as new pairs of solutions $(\tilde{k}_1^{(p)}, \tilde{k}_2^{(p)})$, with $p = 1, 2$ for $\gamma > 4$. Notice that for $\gamma > 4$ all the three solutions are formed by complex conjugated momenta, i.e., $\tilde{k}_1^{(p)} = (\tilde{k}_2^{(p)})^*$ for any p.

5.2 Numerical solution of the Bethe-Gaudin-Takahashi (BGT) equation

The numerical results of the previous section showed that extracting the full set of solutions of the Bethe equations can be a challenging task, as expected. Here we focus on the solutions of the Bethe equations forming the diffusive band (see Fig. 2 and section 3.5). These
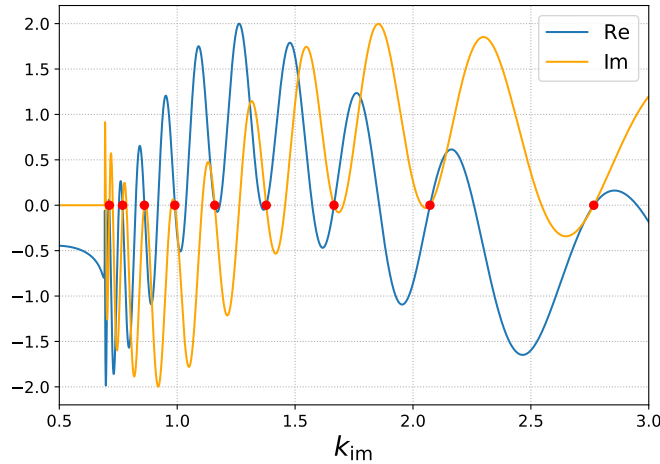
Figure 5: Numerical solution of the BGT equation (37) for a fermionic chain with $L = 10$ and $\gamma = 5$ and $\gamma^- = 0$. The two curves show the real and imaginary parts of (37), plotted versus the imaginary part k_{im} of the quasimomenta k_1, k_2. The circles are the solutions of the BGT equations. Notice that there are $L - 1$ solutions. The missing solution gives $\varepsilon = 0$, and it corresponds to $k_{\mathrm{im}} \to \infty$.

solutions dominate the long-time behavior of physical observables, such as the fermion correlator G_{x_1,x_2}. In the limit of large L, one can use the string hypothesis [52]. Thus, the solutions of the Bethe equations forming the diffusive band are well approximated by the solutions of the Bethe-Gaudin-Takahashi equation (37). Solving (37) is a much simpler task because Eq. (37) is only function of k_{im}, which is real. Importantly, by using the BGT equation in logarithmic form (40) and by varying the quantum numbers I_j, one can target the different momentum pairs (k_1, k_2) forming the diffusive band.

Here we focus on the numerical solution of the BGT equation (37). In Fig. 5 we plot the real and imaginary parts (curves with different colors) of (37) for a chain with $L = 10$, $\gamma = 5$ and $\gamma^- = 0$. On the x-axis k_{im} is the imaginary part of $k_1 = k_2^*$. The real part is obtained from (35). The simultaneous crossing (full circles) of the two curves with the horizontal axis marks the solutions of the BGT equation. Notice that there are $L - 1$ solutions. The missing solution is that with $\varepsilon = 0$. This is present only for $\gamma^- = 0$ and it corresponds to diverging k_1, k_2. Let us now investigate the effect of the losses. In Fig. 6 we show the numerical solutions of (37) for $L = 10$, $\gamma = 5$ and $\gamma^- = 1$. Now, there are L solutions. The solution with $\varepsilon = 0$ is not present. Interestingly, the leftmost circle in Fig. 6 corresponds to two almost degenerate solutions of (37). These are the boundary-related eigenvalues of $\mathcal{L}^{(2)}$ discussed in section 3.5. These boundary states are present only for $\gamma^- > \exp(-\mathrm{arccosh}(\gamma/4))$. Upon lowering γ^- they merge with the diffusive band (cf. 2). The inset of Fig. 6 shows a zoom of the real and imaginary parts of the BGT equation (37) around the two degenerate solutions (leftmost circle in the main Figure). For $L = 10$ the difference between the two solutions is $\mathcal{O}(10^{-4})$.

5.3   Spectrum of the Liouvillian $\mathcal{L}^{(2)}$: Overview

Here we illustrate the general structure of the spectrum of the Liouvillian $\mathcal{L}^{(2)}$ for a fermionic chain with open boundary conditions with $\gamma^- = 0$ as a function of γ. In Fig. 7 we report exact diagonalization results for a chain with $L = 20$ and no boundary losses, i.e., with $\gamma^- = 0$. First, for $\gamma = \gamma^- = 0$ the L^2 energies ε are purely imaginary (not shown in the Figure). Indeed, for $\gamma = 0$, k_1, k_2 are solutions of (24) and (25) with $\gamma^- = 0$,
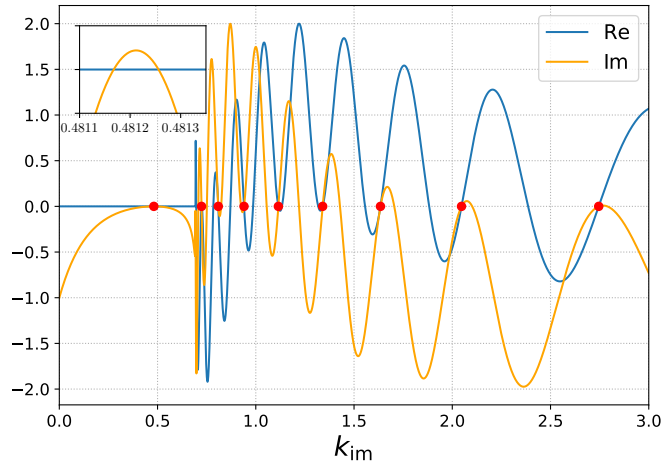
Figure 6: Same as in Fig. 5 for $\gamma^- = 1$. Now there are $L - 2$ solutions within the diffusive band. The solution with $\varepsilon = 0$ is not present for nonzero γ^-. The two almost degenerate solutions at $k_{\mathrm{im}} \approx 0.5$ (see inset in the Figure) correspond to the boundary-related eigenvalues of the Liouvillian (star symbol in Fig. 2 (b)).
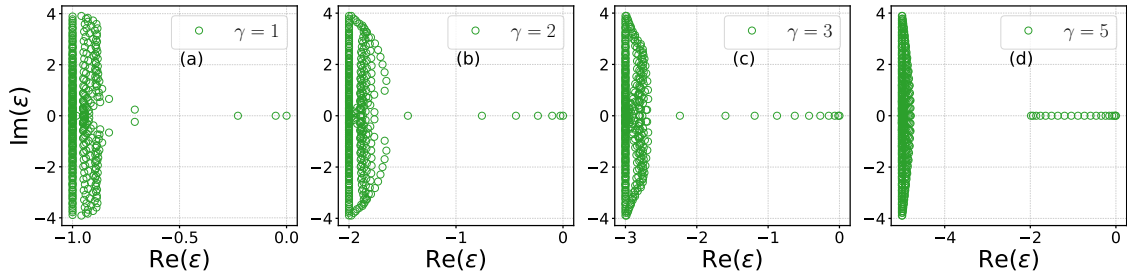
Figure 7: Spectrum of the Liouvillian $\mathcal{L}^{(2)}$ for a fermionic chain with bulk dephasing and no boundary losses, i.e., $\gamma^- = 0$. The symbols are exact diagonalization results for $L = 20$. We plot $\mathrm{Im}(\varepsilon)$ versus $\mathrm{Re}(\varepsilon)$. The different panels show different values of γ. As one increases γ (from left to right in the Figure), the diffusive band with real energies gets populated and well separated from the rest of the spectrum.

and are real. As a consequence the energies ε (cf. (11)) are imaginary. As discussed in section 3.3, at finite γ there are $L(L-1)/2$ momentum pairs (k_1, k_2) that remain the same as for $\gamma = 0$. This implies that the energies ε are the same as for $\gamma = 0$, apart from a trivial shift by $-\gamma$ (cf. (11)). These energies correspond to the vertical straight lines with $\mathrm{Re}(\varepsilon) = -\gamma$ in the different panels. Near this vertical lines there are $\sim L(L-1)/2$ energies that depend in a nontrivial way on γ. These energies correspond to complex solutions of the Bethe equations (18) and (19) with vanishing imaginary parts in the limit $L \to \infty$. For large L these energies can be understood perturbatively in $1/L$, as it was discussed in section 3.4, at least for large enough γ. Finally, upon increasing γ a band of real energies appear. This band contains the energies that are responsible for the diffusive spreading of particles at long times. A similar band appears in the tight-binding chain with periodic boundary conditions [26], and for the periodic tight-binding chain subject to incoherent hopping [28]. As γ increases, the separation in energy between the diffusive band and the remaining part of the spectrum increases. Similar separation in different connected components of the Liouvillian spectrum has been observed in random Liouvillians [55]. As discussed in section 3.5, at $\gamma > 4$ the diffusive band contains at least $L - 2$ states, whereas
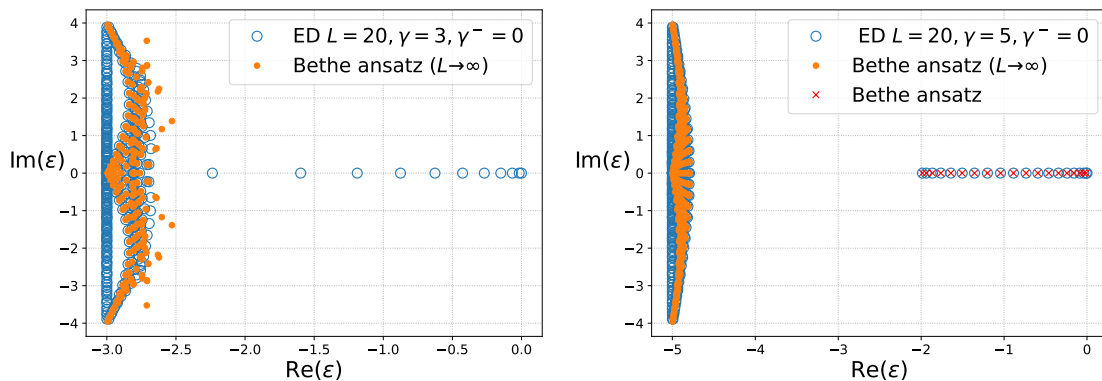
Figure 8: Spectrum of the Liouvillian $\mathcal{L}^{(2)}$ for the open fermionic chain with $L = 20$ and $\gamma^- = 0$. The left (right) panel shows exact diagonalization results (circles) for $\gamma = 3$ ($\gamma = 5$). In both panels a vertical band of $L(L-1)/2$ energies is present at $\varepsilon = -\gamma$. These energies are the same as for $\gamma^- = 0$, apart from a trivial shift by $-\gamma$. Near the vertical band a connected region with $\sim L^2/2$ energies is present. This correspond to the complex solutions of the Bethe equations with vanishing imaginary parts (see section 3.4). Finally, a diffusive band of real energies is also visible in both panels. For $\gamma = 5$ (right panel) the diffusive band is well separated from the rest of the spectrum, and it contains L states. The large L expansion (30) and (31) is reported in both panels with the full circles. The expansion describes well the energies near the vertical band. The crosses in the right panel are Bethe ansatz results obtained by solving numerically (32) and (33) using the solutions of the BGT equation (40) as initial guess.

the number of states diminishes upon lowering γ. These energies in the diffusive band correspond to string solutions of the Bethe equations (18) and (19), and can be effectively treated within the framework of the string hypothesis (see section 3.5).

5.4   Spectrum of $\mathcal{L}^{(2)}$: Exact diagonalization versus Bethe ansatz

Let us now compare the Bethe ansatz results for the energies ε of the Liouvillian $\mathcal{L}^{(2)}$ and exact diagonalization (ED) data. In Fig. 8 we show ED data for $L = 20$, $\gamma^- = 0$ and $\gamma = 3$ and $\gamma = 5$ (left and right panel, respectively). In both panels there is a vertical band containing $L(L-1)/2$ energies. These are the same, except for a trivial shift by $-\gamma$, as for the open fermionic chain with $\gamma = 0$. At small energies the diffusive band of real energies is visible. The complex energies ε between the diffusive band and the vertical band correspond to complex solutions of the Bethe equations with vanishing imaginary parts in the limit $L \to \infty$. As discussed in section 3.4 these eigenvalues of $\mathcal{L}^{(2)}$ can be understood perturbatively in $1/L$. The full circles in the Figure are obtained from the large L expansions (30) and (31). Fig. 8 shows that the large L expansion works well at $\gamma = 5$, i. e., when the diffusive band is well separated from the rest of the spectrum. However, when the diffusive band overlaps with the other regions of the spectrum, the agreement between the large L expansions and the ED data is not perfect.

For $\gamma = 5$ in Fig. 8 we report with the crosses the Bethe ansatz results for the energies of the diffusive band. As it was stressed in section 5.1, extracting the full set of solutions of the Bethe equations is a challenging task. A convenient strategy for the diffusive band is to first solve the BGT equation (37), and then use the solutions as initial guess to solve (18) and (19). The agreement between the Bethe ansatz results and the ED data is perfect. A similar agreement is found for $\gamma = 3$, although we do not report the results
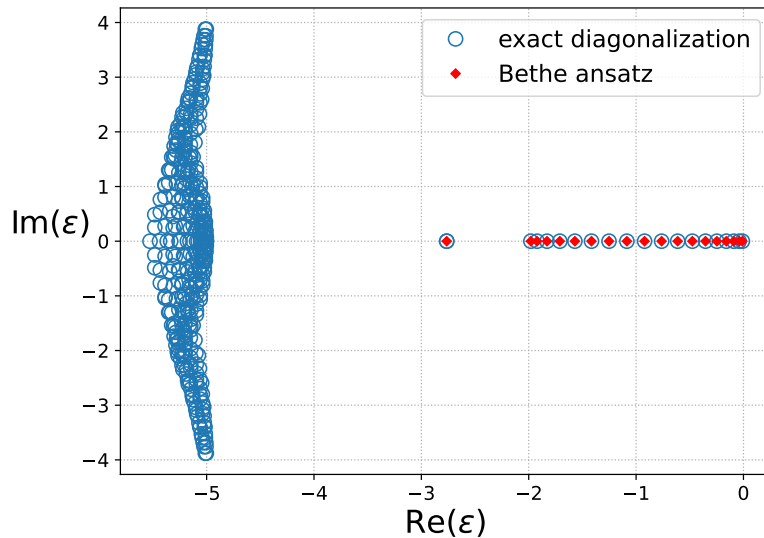
Figure 9: Same as in Fig. 8 for $L = 20$, and $\gamma = 5$ and $\gamma^- = 1$. The diffusive band with $\varepsilon > \sqrt{\gamma^2 - 16} - \gamma$ contains $L - 2$ solutions. An isolated doublet of quasi-degenerate energies is present at $\varepsilon \approx -2.7$, and it corresponds to the boundary-related energies in Fig. 2 (b) (see full diamond symbol in the Figure). The empty circles in the Figure are exact diagonalization (ED) results. The diamonds are the results obtained by solving the BGT equation (37) numerically.

in the Figure. Finally, let us discuss the effect of γ^-. In Fig. 9 we show ED results for $L = 20$, $\gamma = 5$ and $\gamma^- = 1$. Now, the vertical band at small energies $\varepsilon \approx -\gamma$ is deformed. Still, there are $L(L-1)/2$ energies that are the same as in the case with $\gamma = 0$, apart from the trivial shift by $-\gamma$. Again, a diffusive band is present at large energies $\varepsilon \approx 0$. The band contains L energies. The full diamonds are the results obtained using the string hypothesis, i.e., by solving the BGT equation (37). The agreement with the ED data is perfect, even at finite γ^- and despite the fact that the BGT equation (37) is valid only in the limit $L \to \infty$. Finally, the real energy at $\varepsilon \approx -2.7$ corresponds to the almost degenerate doublet of boundary-related eigenvalues of the Liouvillian (see section 3.5), which appear for $\gamma^- > \exp(-\text{arccosh}(\gamma/4))$.

5.5 Finite-size scaling of the Liouvillian gap

Let us now discuss the finite-size scaling of the gap of the Liouvillian $\mathcal{L}^{(2)}$. The Liouvillian gap $\Delta\mathcal{L}^{(2)}$ is the eigenvalue of $\mathcal{L}^{(2)}$ with the largest *nonzero* real part, i.e.,

$$\Delta\mathcal{L}^{(2)} := \max_j \text{Re}(\varepsilon_j), \quad \text{with } \text{Re}(\varepsilon_j) \neq 0. \tag{77}$$

As it is clear from Fig. 8 and Fig. 9, the gap coincides with the largest nonzero energy in the diffusive band. For $\gamma^- = 0$ and in the large L limit the gap is obtained by solving the BGT equation (40) with $I_j = 1$. For $\gamma^- > 0$ one has to fix $I_j = 0$ in (40). In Fig. 10 we plot the Liouvillian gap as a function of L. We show results for $\gamma = 3, 5$ and $\gamma^- = 0, 1$. The symbols are the exact numerical data obtained from the BGT equation (40). The dashed-dotted lines are the results (44) in the large L limit. The leading behavior as $\propto 1/L^2$ is visible. Notice that although Eq. (44) was derived for the case with nonzero γ^- (see section 3.5), it works also for $\gamma^- = 0$. In the inset in Fig. 10 we focus on subleading terms, subtracting from $\Delta\mathcal{L}^{(2)}$ the leading $1/L^2$ behavior (cf. (44)). Precisely, we plot
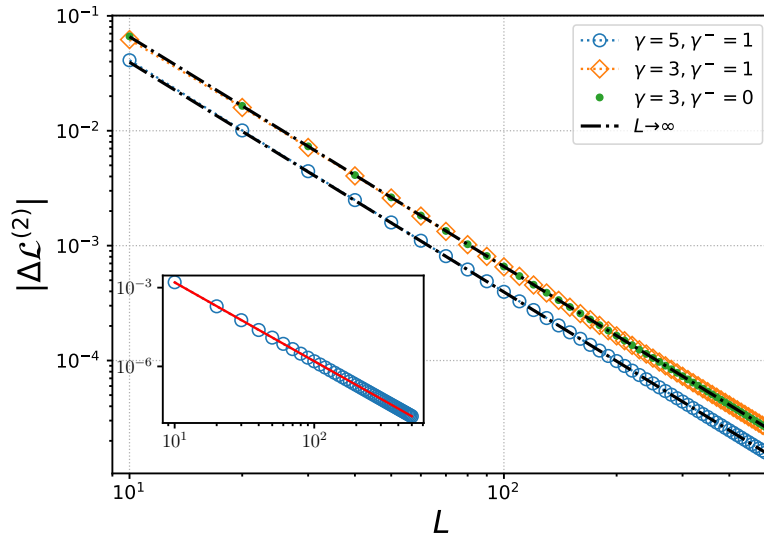
Figure 10: Finite-size scaling of the Liouvillian gap defined in (77). We show results for several values of the dephasing rate γ and boundary loss rate γ^- (different symbols in the Figure). We consider chains with $L \lesssim 500$. The dashed-dotted line is the Bethe ansatz prediction (44) in the limit $L \to \infty$. In the inset we focus on the subleading contributions to the gap for the case with $\gamma = 5$ and $\gamma^- = 1$. The symbols are $\Delta\mathcal{L}^{(2)} + 2\pi^2/(\gamma L^2)$ plotted versus L. The continuous line is the analytic prediction (cf. second term in (44)).

$\Delta\mathcal{L}^{(2)} + 2\pi^2/(\gamma L^2)$ versus L. We only consider the case with $\gamma = 5$ and $\gamma^- = 1$. The continuous line is the second term in (44), which perfectly matches the data.

5.6 Dynamics of the fermionic correlator: Bethe ansatz versus exact diagonalization

Having compared Bethe ansatz versus exact diagonalization results for the spectrum of the Liouvillian, we now focus on the time-dependent fermionic correlator $G_{x_1,x_2}(t)$. Here we compare ED data versus Bethe ansatz results for the *full* correlator G_{x_1,x_2}. The circles in Fig. 11 are ED data for a chain with $L = 10$ sites, $\gamma = 5$, and $\gamma^- = 1$. The results are at fixed time $t = 20$. The left and right panels in the Figure show $\mathrm{Re}(G_{x_1,x_2})$ and $\mathrm{Im}(G_{x_1,x_2})$, respectively. Notice that on the y-axis we employ a logarithmic scale. The numbers on the real axis label the different matrix elements of G_{x_1,x_2}. The full diamonds are Bethe ansatz results. Precisely, here we obtain the full-time dynamics of G_{x_1,x_2} by using the expansion (46). However, since finding all the solutions of the Bethe equations (18) and (19) is a daunting task, we truncate (46) restricting the sum over the energies in the diffusive band, which is expected to dominate the long-time behavior of the correlator. We first numerically solve the BGT equation (40), using the solutions as initial guess for the exact Bethe equations (18) and (19). As it is clear from Fig. 11, the agreement between the Bethe ansatz and the exact diagonalization data is quite satisfactory. Deviations are present for the smaller matrix elements, and can be attributed to the complex eigenvalues ε of the Liouvillian, which we are neglecting.

5.7 Dynamics of the density profile

Here we address the long-time limit of the fermionic density profile, i.e., the diagonal correlators $G_{x,x}$. This is investigated in Fig. 12. In the left and right panels we show the
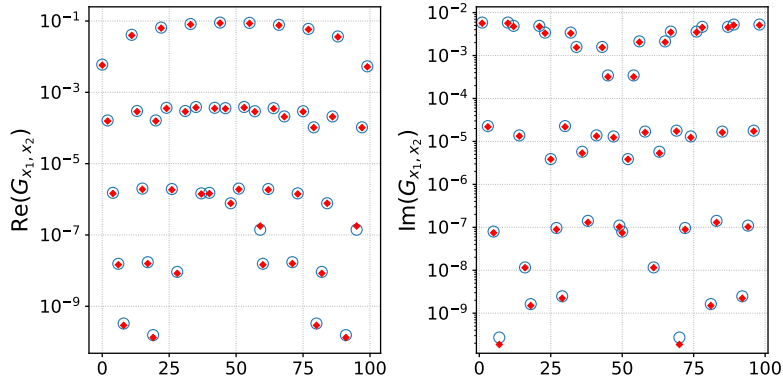
Figure 11: Fermionic correlator G_{x_1,x_2} as a function of time t. The left and right panels show the real and imaginary parts of the correlator, respectively. The initial condition is $G_{x_1,x_2} = \delta_{x_1,L/2}\delta_{x_2,L/2}$. The empty circles are exact diagonalization (ED) results for the matrix elements of G_{x_1,x_2} at $t = 20$. Results are for a chain with $L = 10$, $\gamma = 5$ and $\gamma^- = 1$. The full diamonds are the Bethe ansatz results. These are obtained by solving the Bethe equations (18) and (19) and using (46), where the sum is restricted to the energies of the diffusive band.

dynamics of $G_{L/2,L/2}$ and $G_{1,1}$, respectively. We focus on a chain with $L = 10$ sites. The data are for $\gamma = 5$ and $\gamma^- = 1$. The circles in the figures are exact diagonalization results. The dashed line is the Bethe ansatz result obtained by using (46), where we restrict the sum to the energies in the diffusive band (see Fig. 9). Importantly, we use the solutions of the Bethe equations (18) and (19). Let us first focus on $G_{L/2,L/2}$. At $t = 0$ one has that $G_{L/2,L2} = 1$, while $G_{L/2,L/2}$ vanishes for $t \to \infty$. The agreement between the ED data and the Bethe ansatz is remarkable. Deviations are visible at short times. This is expected because of the truncation in (46). At short times the contribution of the complex energies of the Liouvillian cannot be neglected. The continuous line in Fig. 12 is obtained by considering in (46) only the contribution of the Liouvillian gap, i.e., the energy ε with the largest nonzero real part. The scenario is slightly different for $G_{1,1}$ (right panel in Fig. 12). Precisely, $G_{1,1}$ is zero at $t = 0$, it increases at later times as the particle initially at $x = L/2$ spreads towards the edges. At long times the dynamics is dominated by the boundary loss, and $G_{1,1}$ vanishes. As for $G_{L/2,L/2}$ the agreement between the ED data and the Bethe ansatz obtained by using the diffusive band states (dashed line) is quite satisfactory, although at intermediate times is only qualitatively accurate. On the other hand, the approximation obtained by restricting the sum in (46) to the Liouvillian gap works only at long times.

The profile of the fermionic density $G_{x,x}$ at fixed time and as a function of x is reported in Fig. 13. We show results for a chain with $L = 10$ and time $t = 20$ (empty circles) and $t = 40$ (empty squares). The full diamonds are Bethe ansatz results obtained from (46) restricting the sum over the states in the diffusive band but using the exact solutions of the Bethe equations (18) and (19). The agreement between the Bethe ansatz and the exact diagonalization data is excellent for any x. The hexagons symbols show the Bethe ansatz results obtained employing the string hypothesis, i.e., by using the results of section 4.3. The agreement with the ED data is satisfactory, although some deviations are visible.
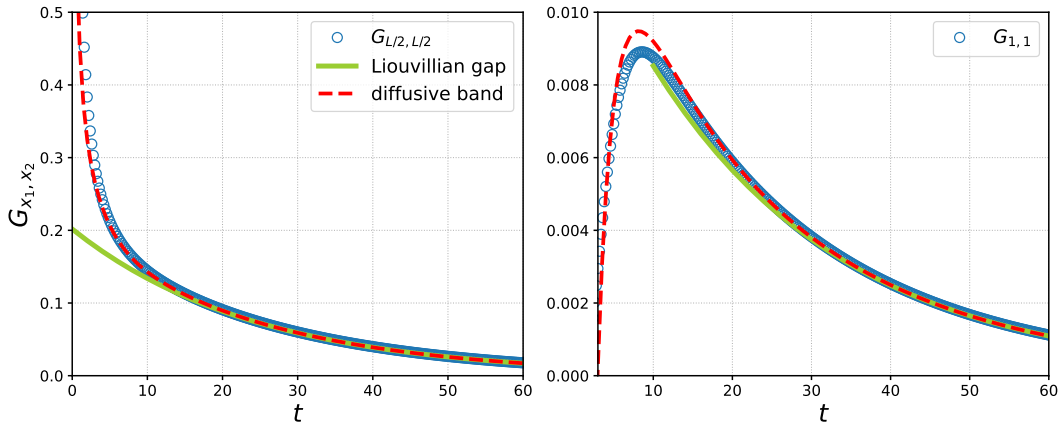
Figure 12: Evolution of the fermionic correlator G_{x_1,x_2} as a function of time t. We show results for a chain with $L = 10$ sites, $\gamma = 5$ and $\gamma^- = 1$. The correlator at $t = 0$ is $G_{x_1,x_2} = \delta_{x_1,L/2}\delta_{x_2,L/2}$, i.e., a fermion localized at the center of the chain. The left and right panels show $G_{L/2,L/2}$ and $G_{1,1}$, respectively. The circles are exact diagonalization data. The dashed line is the Bethe ansatz result obtained by solving numerically the Bethe equations (18) and (19), and using (9). In evolving G_{x_1,x_2} we only considered the energies in the diffusive band (see Fig. 2), which explains the deviations from the ED data. The continuous line is the result considering only the energy with the largest nonzero real part.

5.8 Diffusive scaling

In the long-time limit the density profile $G_{x,x}$ should exhibit diffusive scaling, at least if time is short enough that we can neglect the effect of the boundary losses. This diffusive behavior is observed in the periodic chain [26]. This is investigated in Fig. 14 focusing on the late-time dynamics of $G_{x,x}$ starting from the initial condition with a fermion localized at the center of the chain. In Fig. 14 (a) we show $G_{x,x}$ as a function of $x - L/2$. The symbols are data at different times, and are obtained by using the results of section 4.3. The data are for a system with $L = 100$ sites. As it is clear from the Figure, the fermion density spreads diffusively as time increases, reaching the boundary of the chain at late times. Precisely, in the diffusive regime $G_{x,x}$ is given by

$$G_{x,x} = \frac{1}{\sqrt{4\pi D t}} \exp\left[-\frac{(x - L/2)^2}{4Dt}\right], \quad D := \frac{2}{\gamma}, \tag{78}$$

with D the diffusion constant, which was derived in Ref. [26]. The diffusive scaling is investigated in Fig. 14 (b), plotting $t^{1/2}G_{x,x}$ versus $(x - L/2)/t^{1/2}$. Up to $t = 80$ all the data collapse on the same curve, which is in perfect agreement with (78). At longer times the effect of the boundary loss is non negligible and the diffusive scaling breaks down. At times $t \gg L^2$ the fermion density is vanishing at the edges of the chain, and the height of the fermionic lump that is left around the center of the chain diminishes with time.

6 Conclusions

We derived the Bethe ansatz for the spectrum of the Liouvillian $\mathcal{L}^{(2)}$, which determines the dynamics of the fermionic correlator G_{x_1,x_2} in the fermionic tight-binding chain in the presence of bulk dephasing and boundary losses. For large enough dephasing, the spectrum of the Liouvillian comprises three different parts. Precisely, there are $L(L-1)/2$ complex
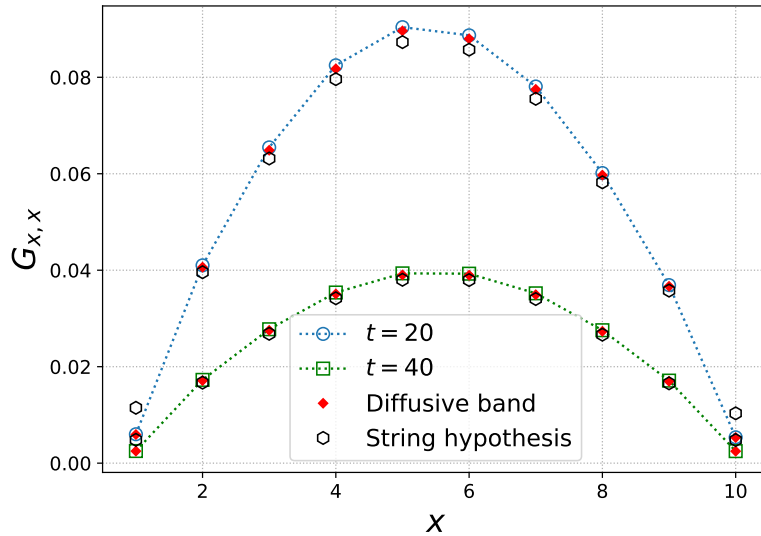
Figure 13: Density profile $G_{x,x}$ plotted as a function of the position x is the chain. The results are for a chain with $L = 10$, dissipation rate $\gamma = 5$ and boundary loss rate $\gamma^- = 1$. The empty circles are exact diagonalization results for $t = 20$ and $t = 40$. At $t = 0$ the correlator is $G_{x_1,x_2} = \delta_{x_1,L/2}\delta_{x_2,L/2}$. The empty hexagons are Bethe ansatz results in the limit $L \to \infty$. These are obtained by solving the BGT equation (40) and using (71). The full diamonds are the same Bethe ansatz results as in Fig. 11.

energies that are trivially related to those of the tight-binding chain with boundary losses and no bulk dephasing. For this reason we dub them dephasing-indepedent energies. Furthermore, there are $\sim L(L-1)/2$ complex energies that are perturbatively related to the dephasing-independent ones in the large chain limit. Finally, there is band of $\sim L$ real energies. Since the band contains the energies with the largest real parts, it dominates the long-time behavior of the correlator, and determines the diffusive scaling at intermediate times. For this reason we dub it diffusive band. Interestingly, for large enough loss rate boundary-related modes of the Liouvillian appear. Both the diffusive band and the boundary modes can be characterized by using the framework of the string hypothesis. Crucially, the Bethe ansatz allowed us to obtain the time-dependent fermionic correlator G_{x_1,x_2}. In particular, we provided analytic formulas for the long-time behavior of the fermionic density $G_{x,x}$.

Let us now illustrate some possible directions for future work. First, we showed that despite the Liouvillian $\mathcal{L}^{(2)}$ being diagonalized by Bethe ansatz, the full Liouvillian is mapped to the Hamiltonian of the open Hubbard chain with boundary magnetic fields and boundary pair production, which is not integrable. It would be interesting to investigate whether the Liouvillian $\mathcal{L}^{(4)}$ that describes the dynamics of the fermionic four point function can be diagonalized by the Bethe ansatz. Furthermore, we showed that at long times the diffusive scaling of the fermionic density is broken, due to the boundary losses. It would be interesting to further investigate this regime to understand whether any universal scaling behavior can be extracted. An interesting direction would be to employ the Bethe ansatz framework to characterize the interplay between dissipation and criticality [2]. This would require to extend the results of section 4 to non-diagonal initial conditions. Recently, it has been shown that several one-dimensional out-of-equilibrium systems exhibit the so-called quantum Mpemba effect [56]. It would be interesting to investigate how the Mpemba effect is affected by dissipation. While this issue has been
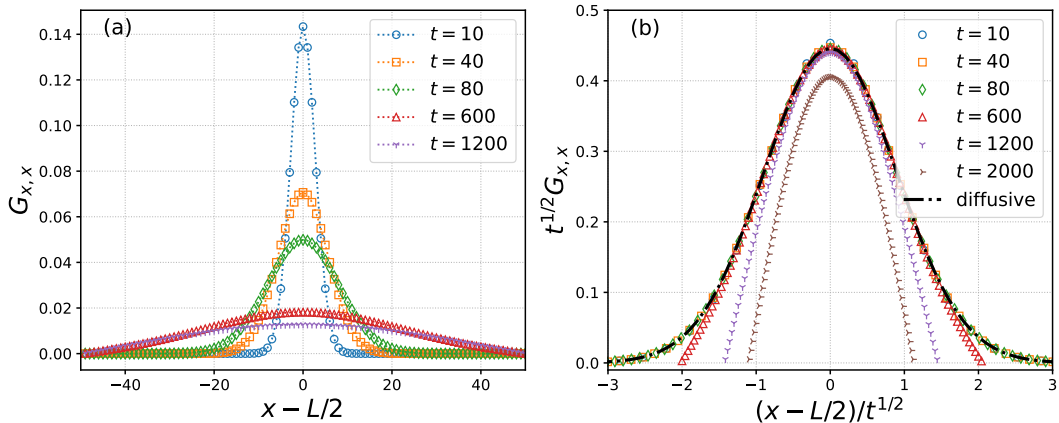
Figure 14: Dynamics of the density profile $G_{x,x}$ for a fermionic chain with $L = 100$, dephasing rate $\gamma = 5$, and boundary loss rate $\gamma^- = 1$. Panel (a) shows the time-dependent correlator $G_{x,x}$ as a function of $x - L/2$. At $t = 0$, $G_{x_1,x_2} = \delta_{x_1,L/2}\delta_{x_2,L/2}$. Panel (b) shows the rescaled density $t^{1/2}G_{x,x}$ as a function of $(x - L/2)/t^{1/2}$. For $t < 600$ the dynamics exhibits a clear diffusive scaling. At later times the boundary losss affect the dynamics, and the diffusive scaling breaks down.

addressed numerically (see for instance Ref. [57]), the Bethe ansatz would allow to clarify the scenario analytically.

The full Liouvillian describing dephasing dissipation is not quadratic in the fermion operators. This implies that entanglement-related quantities are not fully determined by the two-point fermionic correlation function, in contrast with quadratic models [58]. Still, it was observed in Ref. [38] that the "entanglement entropies" defined from the fermionic correlator exhibit scaling behavior in the weak-dissipation hydrodynamic limit. Our results could allow to clarify the origin of this scaling. Finally, it would be important to understand whether the tight-binding chain with localized dephasing can be solved by Bethe ansatz, paving the way to characterize analytically entanglement scaling [43, 44, 59, 60].

Acknowledgements

I would like to thank Yuan Miao for useful discussions. I would also like to thank the Kavli Institute for the Physics and Mathematics of the Universe (Kavli IPMU), where part of this work was completed, for the kind hospitality.

A   Derivation of the full Liouvillian

Here we derive the full Liouvillian $\mathcal{L}$ governing the evolution of the density matrix ρ (cf. (2)). We employ the formalism of the third quantization [7]. This will allow us to map the Liouvillian to a one-dimensional system of spinful fermions described by a Hubbard-like Hamiltonian. In section A.1 we compare the result with the Hamiltonian of the one-dimensional Hubbard model with boundary magnetic fields.

The action of the Liouvillian on a generic density matrix can be understood by using the formalism of Ref. [7]. A generic density matrix can be decomposed as a superposition

of strings of Majorana operators $\Gamma_{\underline{\nu}}$ defined as

$$\Gamma_{\underline{\nu}} := a_1^{\nu_1} a_2^{\nu_2} \cdots a_{2L}^{\nu_{2L}}, \tag{79}$$

where a_j are Majorana fermionic operators with standard anticommutation relations $\{a_j, a_k\} = 2\delta_{jk}$, and $\nu_j = 0, 1$ occupation numbers. The string of operators in (79) is *ordered*. The relationship between Majorana fermions a_j and Dirac fermions c_j is given as

$$a_{2j-1} = c_j + c_j^\dagger, \quad a_{2j} = i(c_j - c_j^\dagger). \tag{80}$$

It is convenient to define the creation and annihilation *super operators* $\hat{a}_j^\dagger$ and $\hat{a}_j$ (notice the hat) acting on $\Gamma_{\underline{\nu}}$ as follows

$$\hat{a}_j^\dagger \Gamma_{\underline{\nu}} = \delta_{\nu_j,0} \pi_j \Gamma_{\underline{\nu}'} \tag{81}$$

$$\hat{a}_j \Gamma_{\underline{\nu}} = \delta_{\nu_j,1} \pi_j \Gamma_{\underline{\nu}'}, \tag{82}$$

where we defined the sign π_j as

$$\pi_j := (-1)^{\sum_{r=1}^{j-1} \nu_j}. \tag{83}$$

In (81) and (82), we defined $\nu_r' = \nu_r$ for $r \neq j$ and $\nu_r' = 1 - \nu_r$ for $r = j$. The super operators $\hat{a}_j, \hat{a}_j^\dagger$ satisfy the standard anticommutation relations of Dirac fermions. First, it is straightforward to check that

$$a_j \Gamma_{\underline{\nu}} = (\hat{a}_j^\dagger + \hat{a}_j) \Gamma_{\underline{\nu}} \tag{84}$$

$$\Gamma_{\underline{\nu}} a_j = (\hat{a}_j^\dagger - \hat{a}_j) \Gamma_{\underline{\nu}}. \tag{85}$$

In (85) we focus on fermionic states with even parity, i.e., for which $\sum_{r=1}^{2L} \nu_r$ is even. By using (84) and (85), one can easily derive the commutation relations

$$[a_j, \Gamma_{\underline{\nu}}] = 2\hat{a}_j \Gamma_{\underline{\nu}} \tag{86}$$

$$[a_j a_k, \Gamma_{\underline{\nu}}] = 2(\hat{a}_j^\dagger \hat{a}_k - \hat{a}_k^\dagger \hat{a}_j) \Gamma_{\underline{\nu}}. \tag{87}$$

For the following, it is convenient to define new fermionic super operators $\hat{a}_{\pm,j}$ as

$$\hat{a}_{\pm,j} := \frac{1}{\sqrt{2}} (\hat{a}_{2m-1} \pm i\hat{a}_{2m}). \tag{88}$$

Notice that $\hat{a}_{\pm,j}$ and $\hat{a}_{+,k}$ act as "creation" or "destruction" super operators. For instance, $\hat{a}_{-,k}$ and $\hat{a}_{+,k}$ destroy the operator $c_k^\dagger$ and c_k, respectively. Similarly, $\hat{a}_{-,k}^\dagger$ and $\hat{a}_{+,k}^\dagger$ create $c_k^\dagger$ and c_k, respectively.

Let us decompose the Liouvillian in (2) in a bulk contribution and in a boundary one as

$$\mathcal{L}(\Gamma_{\underline{\nu}}) = \mathcal{L}_{\text{bulk}}(\Gamma_{\underline{\nu}}) + \mathcal{L}_{\text{boundary}}(\Gamma_{\underline{\nu}}), \tag{89}$$

where $\mathcal{L}_{\text{bulk}}$ contains the Hamiltonian part and the dephasing contribution, whereas $\mathcal{L}_{\text{boundary}}$ takes into account the boundary losses. Specifically, the bulk Liouvillian is given as [11,38]

$$\mathcal{L}_{\text{bulk}} = i \sum_{j=1}^{L-1} \sum_{\alpha=\pm} \alpha (\hat{a}_{\alpha,j}^\dagger \hat{a}_{\alpha,j+1} + \hat{a}_{\alpha,j+1}^\dagger \hat{a}_{\alpha,j})$$

$$+ \frac{\gamma}{2} \sum_{j=1}^{L} (2\hat{a}_{+,j}^\dagger \hat{a}_{+,j} \hat{a}_{-,j}^\dagger \hat{a}_{-,j} - \hat{a}_{+,j}^\dagger \hat{a}_{+,j} - \hat{a}_{-,j}^\dagger \hat{a}_{-,j}), \tag{90}$$

where $\hat{a}_{\pm,j}$ are defined in (88). Let us discuss the boundary term $\mathcal{L}_{\text{boundary}}$. Its action on a generic string Γ_ν reads as

$$\mathcal{L}_{\text{boundary}}(\Gamma_\nu) = \gamma^- \left(c_1 \Gamma_\nu c_1^\dagger - \frac{1}{2}\{c_1^\dagger c_1, \Gamma_\nu\} \right) + c_1 \to c_L, \tag{91}$$

where c_j are Dirac fermions. By using (84) and (85), Eq. (91) is rewritten as

$$\mathcal{L}_{\text{boundary}} = -\frac{\gamma^-}{2}\hat{a}_1^\dagger \hat{a}_1 - \frac{\gamma^-}{2}\hat{a}_2^\dagger \hat{a}_2 + i\gamma^- \hat{a}_1^\dagger \hat{a}_2^\dagger + (\hat{a}_1, \hat{a}_2) \to (\hat{a}_{L-1}, \hat{a}_L). \tag{92}$$

Finally, by using the definition of $\hat{a}_{+,j}$ and $\hat{a}_{-,j}$ in (88), we can rewrite (92) as

$$\mathcal{L}_{\text{boundary}} = -\frac{\gamma^-}{2}\hat{a}_{+,1}^\dagger \hat{a}_{+,1} - \frac{\gamma^-}{2}\hat{a}_{-,1}^\dagger \hat{a}_{-,1} - \gamma^- \hat{a}_{-,1}^\dagger \hat{a}_{+,1}^\dagger + \hat{a}_{\pm,1} \to \hat{a}_{\pm,L}. \tag{93}$$

Now the first two terms in (93) are interpreted as boundary magnetic fields in the Hubbard chain. The last term, however, corresponds to creation of a pair of fermions with opposite spins at the boundary.

Before proceeding, we should observe that to map $\mathcal{L}$ to a Hubbard-like Hamiltonian H as in Ref. [11] we have to perform a unitary transformation as

$$H = i\mathcal{U}^\dagger \mathcal{L} \mathcal{U}, \tag{94}$$

where the unitary transformation $\mathcal{U}$ is defined as [11]

$$\mathcal{U} = \prod_{\text{odd } j} (1 - 2\hat{a}_{-,j}^\dagger \hat{a}_{-,j}). \tag{95}$$

The effect of (95) is to change the sign of the term with $\alpha = -1$ in (90). Finally, the Liouvillian is mapped to the Hubbard-like Hamiltonian H as

$$H = -\sum_{j=1}^{L-1}\sum_{\sigma=\uparrow,\downarrow}(c_{j,\sigma}^\dagger c_{j+1,\sigma} + h.c.) + i\gamma\sum_j n_{j,\uparrow}n_{j,\downarrow} - i\frac{\gamma}{2}\sum_j(n_{j,\uparrow} + n_{j,\downarrow})$$
$$- i\frac{\gamma^-}{2}(n_{1,\uparrow} + n_{1,\downarrow} + n_{L,\uparrow} + n_{L,\downarrow}) + i\gamma^-(c_{1,\uparrow}^\dagger c_{1,\downarrow}^\dagger + (-1)^{L+1}c_{L,\uparrow}^\dagger c_{L,\downarrow}^\dagger), \tag{96}$$

where we redefined $c_{j,\uparrow} := \hat{a}_{+,j}$ and $c_{j,\downarrow} := \hat{a}_{-,j}$. Now, the Hamiltonian (96) is similar to that of the Hubbard chain with boundary magnetic fields. Precisely, Eq. (96) describes a chain of spinful fermions with imaginary density-density interaction, imaginary boundary fields. Crucially, the last term in (96) describes creation of pairs of fermions with opposite spins at the boundary of the chain. To the best of our knowledge, the boundary pair-production term renders the Hamiltonian (96) not integrable.

However, after including a boundary fermion pump term with pump rate $\gamma^+ = \gamma^-$, which is described by the Lindblad operators $L_{x,3} = \sqrt{\gamma^+}c_x^\dagger \delta_{x,1}$ and $L_{x,4} = \sqrt{\gamma^+}c_x^\dagger \delta_{x,L}$, the last term in (93) cancels out. As it was observed in Ref. [11], the resulting Hamiltonian is that of the open Hubbard chain with imaginary interactions and imaginary boundary magnetic fields, which is integrable [25].

A.1 Comparison with the Hubbard model with boundary fields

Although Eq. (96) is not integrable in general, as we showed in section 3, the Liouvillian $\mathcal{L}^{(2)}$ can be diagonalized by the Bethe ansatz. In this section we report the Bethe equations

for the open Hubbard chain with boundary magnetic fields. We show that in the two-fermion sector the Bethe equations are the same as the ones derived in section 3 after some appropriate transformations.

The Hamiltonian of the one-dimensional Hubbard chain with open boundary conditions read as [25]

$$
H = -\sum_{j=1}^{L-1} \sum_{\sigma=\uparrow,\downarrow} (c_{j,\sigma}^\dagger c_{j+1,\sigma} + h.c.) + 4u \sum_j n_{j,\uparrow} n_{j,\downarrow} - 2u \sum_j (n_{j,\uparrow} + n_{j,\downarrow})
$$
$$
- p(n_{1,\uparrow} + n_{1,\downarrow}) - p'(n_{L,\uparrow} + n_{L,\downarrow}), \quad (97)
$$

where $c_{j,\sigma}$ are spinful fermionic operators, $n_{j,\sigma} := c_{j,\sigma}^\dagger c_{j,\sigma}$ is the local fermionic density, u is the interaction strength, and p, p' is the strength of the boundary fields. Eq. (97) is the same as (96) after redefining $u = i\gamma/4$ and $p = i\gamma^-/2$, except for the last term in (96). The Bethe equations for the quasimomenta k_j read as [25]

$$
e^{2ik_j L} \frac{e^{ik_j} - p}{1 - pe^{ik_j}} \frac{e^{ik_j} - p'}{1 - p'e^{ik_j}} = \prod_{\ell=1}^M \frac{\sin(k_j) - \lambda_\ell + iu}{\sin(k_j) - \lambda_\ell - iu} \frac{\sin(k_j) + \lambda_\ell + iu}{\sin(k_j) + \lambda_\ell - iu}, \quad (98)
$$

where $j = 1, \ldots, N$, together with

$$
\prod_{j=1}^N \frac{\lambda_\ell - \sin(k_j) + iu}{\lambda_\ell - \sin(k_j) - iu} \frac{\lambda_\ell + \sin(k_j) + iu}{\lambda_\ell + \sin(k_j) - iu} = \prod_{m=1,m\neq j}^M \frac{\lambda_\ell - \lambda_m + 2iu}{\lambda_\ell - \lambda_m - 2iu} \frac{\lambda_\ell + \lambda_m + 2iu}{\lambda_\ell + \lambda_m - 2iu}, \quad (99)
$$

with $\ell = 1, \ldots, M$, and N, M integers. The energies ε of the eigenstates are given as

$$
\varepsilon = -\sum_{j=1}^N (2\cos(k_j) + 2u). \quad (100)
$$

Now, we are interested in the case with $N = 2$ and $M = 1$. As it is clear from the case of the tight-binding chain with periodic boundary conditions and bulk dephasing, the spectrum of the Hubbard chain with $N = 2$ and $M = 1$ is mapped to the spectrum of $\mathcal{L}^{(2)}$. To proceed, we can solve (100) for λ_1 to obtain

$$
\lambda_1 = \pm\frac{1}{\sqrt{2}} (\sin^2(k_1) + \sin^2(k_2) + 2u^2)^{\frac{1}{2}}. \quad (101)
$$

After substituting (101) in (98), we obtain

$$
e^{2ik_1 L} \frac{e^{ik_1} - p}{1 - pe^{ik_1}} \frac{e^{ik_1} - p'}{1 - p'e^{ik_1}} = \frac{\sin(k_1) - \sin(k_2) + 2iu}{\sin(k_1) - \sin(k_2) - 2iu} \frac{\sin(k_1) + \sin(k_2) + 2iu}{\sin(k_1) + \sin(k_2) - 2iu} \quad (102)
$$

$$
e^{2ik_2 L} \frac{e^{ik_2} - p}{1 - pe^{ik_2}} \frac{e^{ik_2} - p'}{1 - p'e^{ik_2}} = \frac{\sin(k_2) - \sin(k_1) + 2iu}{\sin(k_2) - \sin(k_1) - 2iu} \frac{\sin(k_2) + \sin(k_1) + 2iu}{\sin(k_2) + \sin(k_1) - 2iu}. \quad (103)
$$

After choosing $p = p' = i\gamma^-/2$ and $u = i\gamma/4$, Eq. (102) and Eq. (103) become the same as (18) (19) if one redefines $k_2 \to k_2 + \pi$.

References

[1] H. P. Breuer and F. Petruccione, *The theory of open quantum systems*, Oxford University Press, Great Clarendon Street (2002).

[2] D. Rossini and E. Vicari, *Coherent and dissipative dynamics at quantum phase transitions*, Physics Reports **936**, 1 (2021), doi:https://doi.org/10.1016/j.physrep.2021.08.003.

[3] Y. Lin, J. P. Gaebler, F. Reiter, T. R. Tan, R. Bowler, A. S. Sørensen, D. Leibfried and D. J. Wineland, *Dissipative production of a maximally entangled steady state of two quantum bits*, Nature **504**(7480), 415 (2013), doi:10.1038/nature12801.

[4] F. Verstraete, M. M. Wolf and J. Ignacio Cirac, *Quantum computation and quantum-state engineering driven by dissipation*, Nature Physics **5**(9), 633 (2009), doi:10.1038/nphys1342.

[5] S. Diehl, E. Rico, M. A. Baranov and P. Zoller, *Topology by dissipation in atomic quantum wires*, Nature Physics **7**(12), 971 (2011), doi:10.1038/nphys2106.

[6] P. Calabrese, F. H. L. Essler and G. Mussardo, *Introduction to 'Quantum Integrability in Out of Equilibrium Systems'*, Journal of Statistical Mechanics: Theory and Experiment **2016**(6), 064001 (2016), doi:10.1088/1742-5468/2016/06/064001.

[7] T. Prosen, *Third quantization: a general method to solve master equations for quadratic open Fermi systems*, New Journal of Physics **10**(4), 43026 (2008), doi:10.1088/1367-2630/10/4/043026.

[8] M. Žnidarič, *Exact solution for a diffusive nonequilibrium steady state of an open quantum chain*, Journal of Statistical Mechanics: Theory and Experiment **2010**(05), L05002 (2010), doi:10.1088/1742-5468/2010/05/l05002.

[9] M. Žnidarič, *Solvable quantum nonequilibrium model exhibiting a phase transition and a matrix product representation*, Phys. Rev. E **83**, 011108 (2011), doi:10.1103/PhysRevE.83.011108.

[10] T. Prosen, *Exact Nonequilibrium Steady State of a Strongly Driven Open XXZ Chain*, Phys. Rev. Lett. **107**, 137201 (2011), doi:10.1103/PhysRevLett.107.137201.

[11] M. V. Medvedyeva, F. H. L. Essler and T. Prosen, *Exact Bethe Ansatz Spectrum of a Tight-Binding Chain with Dephasing Noise*, Phys. Rev. Lett. **117**, 137202 (2016), doi:10.1103/PhysRevLett.117.137202.

[12] E. Ilievski, *Dissipation-driven integrable fermionic systems: from graded Yangians to exact nonequilibrium steady states*, SciPost Phys. **3**, 031 (2017), doi:10.21468/SciPostPhys.3.4.031.

[13] B. Buča, C. Booker, M. Medenjak and D. Jaksch, *Bethe ansatz approach for dissipation: exact solutions of quantum many-body dynamics under loss*, New Journal of Physics **22**(12), 123040 (2020), doi:10.1088/1367-2630/abd124.

[14] F. H. L. Essler and L. Piroli, *Integrability of one-dimensional lindbladians from operator-space fragmentation*, Phys. Rev. E **102**, 062210 (2020), doi:10.1103/PhysRevE.102.062210.

[15] A. A. Ziolkowska and F. H. Essler, *Yang-Baxter integrable Lindblad equations*, SciPost Phys. **8**, 44 (2020), doi:10.21468/SciPostPhys.8.3.044.

[16] J. Robertson and F. H. L. Essler, *Exact solution of a quantum asymmetric exclusion process with particle creation and annihilation*, Journal of Statistical Mechanics: Theory and Experiment **2021**(10), 103102 (2021), doi:10.1088/1742-5468/ac22f8.

[17] M. Nakagawa, N. Kawakami and M. Ueda, *Exact Liouvillian Spectrum of a One-Dimensional Dissipative Hubbard Model*, Phys. Rev. Lett. **126**, 110404 (2021), doi:10.1103/PhysRevLett.126.110404.

[18] K. Yamamoto, M. Nakagawa, M. Tezuka, M. Ueda and N. Kawakami, *Universal properties of dissipative Tomonaga-Luttinger liquids: Case study of a non-Hermitian XXZ spin chain*, Phys. Rev. B **105**, 205125 (2022), doi:10.1103/PhysRevB.105.205125.

[19] N. Shibata and H. Katsura, *Quantum Ising chain with boundary dephasing*, Progress of Theoretical and Experimental Physics **2020**(12), 12A108 (2020), doi:10.1093/ptep/ptaa131, https://academic.oup.com/ptep/article-pdf/2020/12/12A108/35415150/ptaa131.pdf.

[20] M. de Leeuw, C. Paletta and B. Pozsgay, *Constructing Integrable Lindblad Superoperators*, Phys. Rev. Lett. **126**, 240403 (2021), doi:10.1103/PhysRevLett.126.240403.

[21] P. W. Claeys and A. Lamacraft, *Dissipative dynamics in open XXZ Richardson-Gaudin models*, Phys. Rev. Res. **4**, 013033 (2022), doi:10.1103/PhysRevResearch.4.013033.

[22] M. de Leeuw and C. Paletta, *The Bethe ansatz for a new integrable open quantum system* (2022), 2207.14193.

[23] H. Yoshida and H. Katsura, *Liouvillian gap and single spin-flip dynamics in the dissipative fermi-hubbard model*, Phys. Rev. A **107**, 033332 (2023), doi:10.1103/PhysRevA.107.033332.

[24] K. Yamanaka and T. Sasamoto, *Exact solution for the Lindbladian dynamics for the open XX spin chain with boundary dissipation*, SciPost Phys. **14**, 112 (2023), doi:10.21468/SciPostPhys.14.5.112.

[25] F. H. L. Essler, H. Frahm, F. Göhmann, A. Klümper and V. E. Korepin, *The One-Dimensional Hubbard Model*, Cambridge University Press, doi:10.1017/CBO9780511534843 (2005).

[26] M. Esposito and P. Gaspard, *Emergence of diffusion in finite quantum systems*, Phys. Rev. B **71**, 214302 (2005), doi:10.1103/PhysRevB.71.214302.

[27] M. Esposito and P. Gaspard, *Exactly solvable model of quantum diffusion*, Journal of Statistical Physics **121**(3), 463 (2005), doi:10.1007/s10955-005-7577-x.

[28] V. Eisler, *Crossover between ballistic and diffusive transport: the quantum exclusion process*, Journal of Statistical Mechanics: Theory and Experiment **2011**(06), P06007 (2011), doi:10.1088/1742-5468/2011/06/P06007.

[29] I. Bouchoule, B. Doyon and J. Dubail, *The effect of atom losses on the distribution of rapidities in the one-dimensional Bose gas*, SciPost Phys. **9**, 44 (2020), doi:10.21468/SciPostPhys.9.4.044.

[30] D. Rossini, A. Ghermaoui, M. B. Aguilera, R. Vatré, R. Bouganne, J. Beugnon, F. Gerbier and L. Mazza, *Strong correlations in lossy one-dimensional quantum gases: From the quantum zeno effect to the generalized gibbs ensemble*, Phys. Rev. A **103**, L060201 (2021), doi:10.1103/PhysRevA.103.L060201.

[31] F. Riggio, L. Rosso, D. Karevski and J. Dubail, *Effects of atom losses on a one-dimensional lattice gas of hardcore bosons* (2023), 2307.02298.

[32] M. Coppola, G. T. Landi and D. Karevski, *Wigner dynamics for quantum gases under inhomogeneous gain and loss processes with dephasing*, Phys. Rev. A **107**, 052213 (2023), doi:10.1103/PhysRevA.107.052213.

[33] G. Perfetto, F. Carollo, J. P. Garrahan and I. Lesanovsky, *Reaction-limited quantum reaction-diffusion dynamics*, Phys. Rev. Lett. **130**, 210402 (2023), doi:10.1103/PhysRevLett.130.210402.

[34] G. Perfetto, F. Carollo, J. P. Garrahan and I. Lesanovsky, *Quantum reaction-limited reaction-diffusion dynamics of annihilation processes* (2023), `2305.06944`.

[35] P. Calabrese and J. Cardy, *Evolution of entanglement entropy in one-dimensional systems*, Journal of Statistical Mechanics: Theory and Experiment **2005**(04), P04010 (2005), doi:10.1088/1742-5468/2005/04/p04010.

[36] M. Fagotti and P. Calabrese, *Evolution of entanglement entropy following a quantum quench: Analytic results for the XY chain in a transverse magnetic field*, Phys. Rev. A **78**, 010306 (2008), doi:10.1103/PhysRevA.78.010306.

[37] V. Alba and P. Calabrese, *Entanglement and thermodynamics after a quantum quench in integrable systems*, Proceedings of the National Academy of Sciences **114**(30), 7947 (2017), doi:10.1073/pnas.1703516114, `https://www.pnas.org/content/114/30/7947.full.pdf`.

[38] V. Alba and F. Carollo, *Spreading of correlations in Markovian open quantum systems*, Phys. Rev. B **103**, L020302 (2021), doi:10.1103/PhysRevB.103.L020302.

[39] F. Carollo and V. Alba, *Dissipative quasiparticle picture for quadratic markovian open quantum systems*, Phys. Rev. B **105**, 144305 (2022), doi:10.1103/PhysRevB.105.144305.

[40] V. Alba and F. Carollo, *Hydrodynamics of quantum entropies in Ising chains with linear dissipation*, Journal of Physics A: Mathematical and Theoretical **55**(7), 74002 (2022), doi:10.1088/1751-8121/ac48ec.

[41] V. Alba and F. Carollo, *Logarithmic negativity in out-of-equilibrium open free-fermion chains: An exactly solvable case* (2022), `2205.02139`.

[42] V. Alba and F. Carollo, *Noninteracting fermionic systems with localized losses: Exact results in the hydrodynamic limit*, Phys. Rev. B **105**, 054303 (2022), doi:10.1103/PhysRevB.105.054303.

[43] V. Alba, *Unbounded entanglement production via a dissipative impurity*, SciPost Phys. **12**, 11 (2022), doi:10.21468/SciPostPhys.12.1.011.

[44] F. Caceffo and V. Alba, *Entanglement negativity in a fermionic chain with dissipative defects: exact results*, Journal of Statistical Mechanics: Theory and Experiment **2023**(2), 023102 (2023), doi:10.1088/1742-5468/acb429.

[45] X. Turkeshi and M. Schiró, *Diffusion and thermalization in a boundary-driven dephasing model*, Phys. Rev. B **104**, 144301 (2021), doi:10.1103/PhysRevB.104.144301.

[46] X. Turkeshi, L. Piroli and M. Schiró, *Enhanced entanglement negativity in boundary-driven monitored fermionic chains*, Phys. Rev. B **106**, 024304 (2022), doi:10.1103/PhysRevB.106.024304.

[47] T. Jin, M. Filippone and T. Giamarchi, *Generic transport formula for a system driven by markovian reservoirs*, Phys. Rev. B **102**, 205131 (2020), doi:10.1103/PhysRevB.102.205131.

[48] T. Jin, J. a. S. Ferreira, M. Filippone and T. Giamarchi, *Exact description of quantum stochastic models as quantum resistors*, Phys. Rev. Res. **4**, 013109 (2022), doi:10.1103/PhysRevResearch.4.013109.

[49] F. Tarantelli and E. Vicari, *Quantum critical systems with dissipative boundaries*, Phys. Rev. B **104**, 075140 (2021), doi:10.1103/PhysRevB.104.075140.

[50] G. T. Landi, D. Poletti and G. Schaller, *Nonequilibrium boundary-driven quantum systems: Models, methods, and properties*, Rev. Mod. Phys. **94**, 045006 (2022), doi:10.1103/RevModPhys.94.045006.

[51] F. C. Alcaraz, M. N. Barber, M. T. Batchelor, R. J. Baxter and G. R. W. Quispel, *Surface exponents of the quantum XXZ, Ashkin-Teller and Potts models*, Journal of Physics A: Mathematical and General **20**(18), 6397 (1987), doi:10.1088/0305-4470/20/18/038.

[52] M. Takahashi, *Thermodynamics of One-Dimensional Solvable Models*, Cambridge University Press, doi:10.1017/CBO9780511524332 (1999).

[53] V. Alba, K. Saha and M. Haque, *Bethe ansatz description of edge-localization in the open-boundary XXZ spin chain*, Journal of Statistical Mechanics: Theory and Experiment **2013**(10), P10018 (2013), doi:10.1088/1742-5468/2013/10/P10018.

[54] C. Guo and D. Poletti, *Analytical solutions for a boundary-driven XY chain*, Phys. Rev. A **98**, 052126 (2018), doi:10.1103/PhysRevA.98.052126.

[55] J. Costa, P. Ribeiro, A. de Luca, T. Prosen and L. Sá, *Spectral and steady-state properties of fermionic random quadratic liouvillians* (2022), `2210.07959`.

[56] F. Ares, S. Murciano and P. Calabrese, *Entanglement asymmetry as a probe of symmetry breaking*, Nature Communications **14**(1), 2036 (2023), doi:10.1038/s41467-023-37747-8.

[57] V. Vitale, A. Elben, R. Kueng, A. Neven, J. Carrasco, B. Kraus, P. Zoller, P. Calabrese, B. Vermersch and M. Dalmonte, *Symmetry-resolved dynamical purification in synthetic quantum matter*, SciPost Phys. **12**, 106 (2022), doi:10.21468/SciPostPhys.12.3.106.

[58] I. Peschel and V. Eisler, *Reduced density matrices and entanglement entropy in free lattice models*, Journal of Physics A: Mathematical and Theoretical **42**(50), 504003 (2009), doi:10.1088/1751-8113/42/50/504003.

[59] A. P. Chaudhari, S. P. Kelly, R. J. Valencia-Tortora and J. Marino, *Zeno crossovers in the entanglement speed of spin chains with noisy impurities*, Journal of Statistical Mechanics: Theory and Experiment **2022**(10), 103101 (2022), doi:10.1088/1742-5468/ac8e5d.

[60] A. D'Abbruzzo, V. Alba and D. Rossini, *Logarithmic entanglement scaling in dissipative free-fermion systems*, Phys. Rev. B **106**, 235149 (2022), doi:10.1103/PhysRevB.106.235149.